PLASMONIC ENHANCEMENT OF PEROVSKITE PHOTOLUMINESCENCE

A Thesis Submitted to
the Graduate School of Engineering and Sciences of
İzmir Institute of Technology
in Partial Fulfillment of the Requirements for the Degree of

MASTER OF SCIENCE

in Photonics Science and Engineering

by
Metin TAN

July 2020
İZMİR

ACKNOWLEDGMENTS

It is my honor to be one of the first graduates of a great person and advisor, Dr. Emre SARI, who supported me with his kind personality from the beginning to end of this graduate education, and whose friendship and thoughts are important to me.

I would like to thank to Prof. Dr. Alev Devrim GÜÇLÜ from Physics Department, who always supported me and answered my questions with his great patience during my scientific preparation in Physics. I believe I would not understand none of what I did during this graduate education if I were not one of his students.

I thank Görkem MUTLU, Teyfik YILMAZ, Ümit PURÇAK, Zeynep KAHRAMAN and Necip Ayhan TERTEMİZ for their fun friendship and being always there for me.

I learnt lots of basics about Photonics from Prof. M. R. SHENOY's online lectures. I could not pass this section without thanking him for his great lecture series.

It is my great pleasure to honor Gabe NEWELL, here. Without his great software, Steam, I would lose my mind.

This thesis is supported by Scientific and Technological Research Council of Turkey (TÜBİTAK).

ABSTRACT

PLASMONIC ENHANCEMENT
OF PEROVSKITE PHOTOLUMINESCENCE

Recently emerged perovskite materials show superior features like high efficiency, defect tolerance, facile synthesis, bandgap tunability and wide color gamut over their rivals in photonics applications. On the other hand, metals have interesting characteristics as they go smaller in size. Their absorption and scattering properties are completely different as nanoparticles. Their confined electron oscillations bring peculiar consequences. Due to change in these features, metallic nanoparticles can enhance or quench fields around them.

Light-matter interactions determine how we see the world. Understanding quantum nature of light and matter and their interactions can benefit higher efficiencies and can open paths for novel technologies. In accordance with this purpose, this thesis study involves synthesis of cesium lead halide perovskite emitters and investigation of their interactions with silver nanoisland films. It was concluded that direct contact between perovskite layer and nanoislands results in a fluorescence quenching where intensity average lifetime decreases below 1 ns. Separating these layers with an alumina dielectric layer increased photoluminescence intensity after 15 nm and the highest intensity was observed at 18 nm thickness with 78% of PL enhancement. With different spacer thickness values, we achieved to see the change in photoluminescence intensity.

ÖZET

PEROVSKİT FOTOIŞIMASININ PLAZMONİK ARTIRIMI

Son zamanlarda ortaya çıkan perovskit malzemeler, fotonik uygulamalarındaki rakiplerine göre yüksek verimlilik, hata toleransı, kolay sentez, bant aralığı ayarlanabilirliği ve geniş renk gamı gibi üstün özellikler göstermektedir. Diğer yandan metaller, boyutları küçüldükçe ilginç özelliklere sahip olur. Nanoparçacık olarak soğurma ve saçılma özellikleri tamamen farklıdır. Kısıtlanan elektron salınımları tuhaf sonuçlar getirir. Bu özelliklerin değişmesi nedeniyle, metalik nanoparçacıklar etraflarındaki alanları kuvvetlendirebilir veya söndürebilir.

Işık-madde etkileşimleri dünyayı nasıl gördüğümüzü belirler. Işığın ve maddenin kuantum doğasını ve bunların etkileşimlerini anlamak, daha yüksek verimlilikleri elde etmeye yarar sağlayabilir ve yeni teknolojiler için yollar açabilir. Bu amaç doğrultusunda, bu tez çalışması, sezyum kurşun halojenür perovskit ışıyıcıların sentezini ve gümüş nanoadacık filmleriyle etkileşimlerinin incelenmesini içermektedir. Perovskit tabakası ile nanoadalar arasındaki doğrudan temasın, ağırlık ortalama ömrün 1 ns'nin altına düştüğü bir floresan söndürme ile sonuçlandığı sonucuna varılmıştır. Bunları katmanları bir alümina dielektrik katmanı ile ayırmak, 15 nm'den sonra fotolüminesans yoğunluğunu arttırdı ve en yüksek yoğunluk,% 78 PL artışıyla 18 nm kalınlıkta gözlendi. Böylelikle, farklı aralayıcı kalınlığı değerleri ile, fotolüminesans yoğunluğundaki değişikliği görmeyi başardık.

Dedicated to good and kind people all over the world…

TABLE OF CONTENTS

LIST OF FIGURES

Figure **Page**

Figure **Page**

LIST OF TABLES

LIST OF ABBREVIATIONS

AFM	Atomic Force Microscopy
Ag	Silver
ALD	Atomic Layer Deposition
Au	Gold
ILHP	Inorganic Lead Halide Perovskite
IR	Infrared
LSP	Localized Surface Plasmon
LSPR	Localized Surface Plasmon Resonance
PLQY	Photoluminescence Quantum Yield
PVD	Physical Vapor Deposition
RMS	Root Mean Square
RV	Reaction Vial
SPP	Surface Plasmon Polariton
SPR	Surface Plasmon Resonance
TMA	Trimethylaluminum
TRPL	Time Resolved Photoluminescence
UV	Ultraviolet
SEM	Scanning Electron Microscope/Microscopy

CHAPTER 1

INTRODUCTION

Understanding the matter has taken our civilization a step further. As soon as we investigated smaller size matters, we understood that there is a different world than the one we live in. The nanoworld is peculiar. Nanosized materials differ from their bulk counterparts. Due to small sizes, charges and photons confined in nanostructures bring strange outcomes that are not observable in bulk materials. Different optical, electronical, magnetic, etc. features of nanoparticles lead the way for applications we cannot imagine otherwise. Therefore, lots of investigations still help us understand the nanoworld better.

Nanostructures like lead halide perovskite nanocrystals emerged as promising materials for light absorbing and emitting applications. The solar cell performance of this materials platform reached close to their theoretical limit in a very small amount of time, whereas emitter counterparts can exhibit near unity photoluminescence quantum yield. Sought after features such as pure color emission through narrow linewidth, defect tolerance, bandgap tunability and wide color gamut announces lead halide perovskite nanocrystals as next generation materials for display applications.

Metal nanostructures, on the other hand, show interesting behaviors by virtue of their free electrons unlike other nanocrystals. Free electrons oscillate in metal surfaces and their quanta is called plasmon. An external electromagnetic field can be enhanced by tens or even thousand times near a metal nanoparticle or any radiation can be quenched with the help of plasmons. According to the size and shape of a metal nanoparticle, different wavelengths of light can be absorbed or scattered, thus metallic particles in different colors can be produced from the same metal atoms.

Today, sensitivity of any device has utmost importance for detection applications. For example, fluorescence of most biomolecules has low intensity or their density in the medium makes their detection difficult. Therefore, fluorescence enhancement mechanisms are needed. Also, low luminescence performance of any light emitting material prevents them to be a candidate for LED applications. When Raman emission is under consideration, again low intensities are encountered. These kinds of issues denote metal nanoparticles as good problem solvers due to enhanced fields around them.

Utilizing proper metal nanoparticles under proper conditions, one can enhance any flurophore's emission rate up to its theoretical limit. For this purpose, metal nanoparticles with several shapes such as nanosphere, nanowire, nanotriangle, nanocubes etc. were snyhtesized before.

Under the spotlight of the interesting world of nanomaterials, in this thesis, we utilize localized surface plasmons which are located in metal nanoislands in order to increase radiative emission rate of lead halide perovskite nanoemitters. By spectrally matching metal absorption and emission peak of perovskites with a very thin dielectric material in between, intensity can be enhanced. Hence, in this work, changing the distance between perovskite nanocrystals and silver nanoisland film layer by using alumina as dielectric spacer, radiative decay rates through time correlated single photon counting and peak emission intensities through photoluminescence were investigated. It was observed that the intensity has a maximum thickness point which decreases after a particular emitter-metal distance, when coupling strength starts to decrease.

This thesis is organized as follows: Chapter 2 describes perovskites and results obtained from recent perovskite studies. In this chapter, advantages of perovskite nanocrystals over their rivals are elaborated with the help of studies from the literature. Also, conditions affecting synthesis process are briefly explained. In Chapter 3, properties of metal nanocrystals are given under Surface Plasmons topic. Effects of plasmons on determining metallic properties and requirements to excite surface plasmons with electromagnetic waves are elaborated theoretically. In addition, field enhancement of metals near particle surfaces are explained. Experimental methods and devices utilized to investigate the material characteristics are mentioned in Chapter 4. The explanation of the working principles and basic schematics of the equipment and microscopy techniques used (such as physical vapor deposition, atomic layer deposition, scanning electron microscope, atomic force microscope and optical spectroscopy systems) and synthesis method are included in this chapter. After giving details on all the necessary equipment, in Chapter 5 experimental process and results, such as deposition methods, effects of changing the parameters used, are elucidated, and commented.

CHAPTER 2

PEROVSKITES

Perovskite is the name of materials having the ABX_3 stoichiometry and named after the Russian mineralogist Lev Alekseyevich Perovski (1792-1856) by the German mineralogist Gustav Rose (1798-1873). [1] At first, the word perovskite was only for a specific material, calcium titanate ($CaTiO_3$) which was determined first. But years later, lots of materials having the same formula has been discovered and the perovskite has become a whole big family.

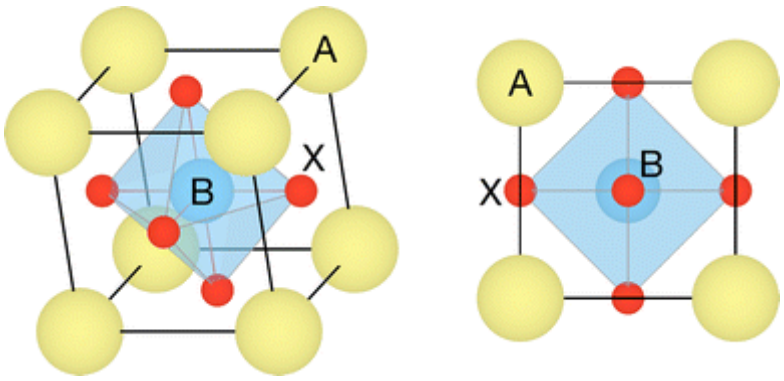

Figure 2.1: Perovskite lattice structure [71]

A simple perovskite structure is given in Figure 1.1. Perovskite family involves several symmetries and various physical properties. These features are ruled by their A^+ and B^{2+} site cations and X^- site anions. According to ions constituting a perovskite, the material can show semiconductivity, magnetism [2-4], dielectricity [5-8], ferroelectricity [9-11], ferroelasticity [12,13] or lasing [14-17,53-56] etc. Tuning synthesis conditions, ingredients, and/or different factors, one can obtain cubic, orthorhombic, trigonal, tetragonal, monoclinic or triclinic symmetries.

This thesis focuses on inorganic lead halide perovskite (ILHP) nanocrystals which are comprised of cesium (Cs) as A^+ site cation, lead (Pb) as B^{2+} site cation and a halogen which can be chloride (Cl), bromide (Br) or iodide (I) as X^- site anion. $CsPbX_3$ perovskites are deeply investigated for remarkably solar harvesting and highly luminescent light emitting properties. Their bandgaps fall in the optic regime and this makes them good candidate for novel light applications.

2.1. Cesium Lead Halide Perovskite Nanocrystals

The first solar harvester was made of silicon with 1% power conversion efficiency (PCE) in 1941 [18]. After its first invention, silicon solar cells have been number one in solar energy market. Record in PCE for silicon solar cells were over 26% in 2017 [19,20] whereas theoretical limit for crystalline silicon solar cells is ~29% [21] and in order to reach this limit, 76 years were required. But for lead halide perovskite solar cells compared with silicon counterparts, comparatively very short time from 2009 was enough to go from %3 [22] to over 20% [23-25] record efficiencies.

Addition to solar applications, first light emission from perovskites was obtained not much time ago. Starting from 1992, perovskite emitters did not achieve strong emission at room temperatures [26]. Due to its weakness, it was not possible to use them as an electroluminescence device. Recently, ILHP nanocrystal emitters are under the spotlight owing to their exceptional characteristics. The tunability of peak wavelength through anion exchange [27-32], facile and ambient condition synthesis methods [33,34] as well as other superior features make ILHP nanocrystals suitable choice for light emitting applications.

Lattice formations observed in ILHP nanocrystals are orthorhombic, tetragonal, and cubic, where different formations may lead to different properties. Having these formations, perovskite nanocrystals can be seen in the form of various nanostructures such as quantum dot, nanowire, nanorod, nanosheet, nanocube, nanoplatelet, etc. It is not always possible to define a perovskite crystal with a completely correct formula because of its defects or grain boundaries. More general formula for an ILHP crystal is $R_2A_{n-1}B_nX_{3n+1}$, where R is a ligand, A is Cs, B is Pb and X is Cl, Br, or I. In this formula, n determines the number of perovskite layers between ligand molecules. While n=1 results in a monolayer perovskite consisting of $[PbX_6]^-$ octahedral structures arranged in a plane, n=∞ gives rise to the well-known formula of perovskites, ABX_3 [37].

Each X^- anion is shared by two octahedrons and this leads to "-1/2" ionic charge contribution per halide ion to the $[PbX_6]$ octahedron. Therefore, every ILHP corner-sharing octahedron has total ionic charge of "-1". Octahedrons located in a perovskite lattice are the core part that establishes the electronic formation, therefore energy levels of the crystal. The valence band consists of np orbitals of X and 6s orbitals of Pb, and the conduction band includes 6p orbitals of Pb and np orbitals of X [38-40]. Therefore, lead halide perovskites have tunable electronic energy band gap changeable by X site element.

Replacing the X site with a larger halogen, i.e. moving from chlorine's 3p orbital to iodine's 5p orbital, causes light emission to shift from near-UV to near-IR [41-44]. Also, alloying different halogens in different ratios gives a continuous shift between two colors. Acquired color gamut this way is wider than the ones obtained with other light sources. Density of states contributions from the highest orbitals of Cs, Pb and Br are given in Figure 1.2 [66]. If the inorganic cesium located in the A site is switched by an organic methylammonium group, it results in a little redshift in the bandgap [45].

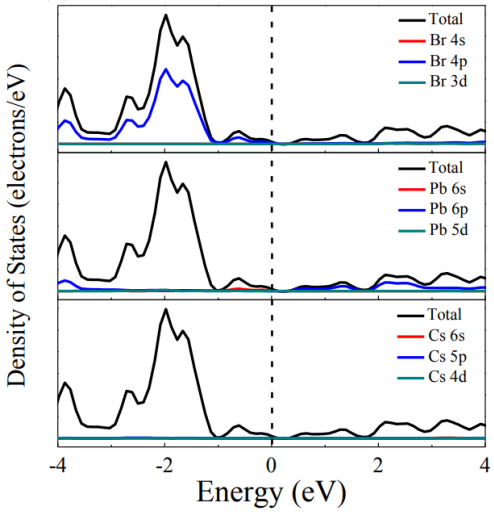

Figure 2.2: Density of states contributions from the highest state orbitals [66]

One of the most important features of lead halide perovskites is that they have a huge defect tolerance. Anti-bonding condition of X's np and Pb's 6s orbitals which determine the valance band and nonbonding condition of X's np and Pb's 6p orbitals which determine the conduction band do not let a bonding-antibonding condition between energy bands, where this leads to a defect tolerant material, because defect sources are mostly seen in A and X sites and these defect states do fall out of the band gap [38,39,46-48]. Having this intrinsic characteristic, ILHPs differ from conventional semiconductors whose energy bands are built by bonding valence and antibonding conduction bands [46,47]. This fine band structure allows ILHP nanocrystals to exhibit a narrow emission even without defect passivation [38,46-48]. Nonetheless, nonradiative recombination still causes low performance in luminescence. Thus, the passivation of defect states and obtaining a crystalline structure are important to achieve higher efficiencies [49-52]. By applying these improvements on ILHP nanocrystals, one can increase photoluminescence quantum yield (PLQY) up to almost unity [57-61].

Narrow emission resulting in pureness of color, color tunability over visible range, better stability than organo-metallic counterparts and high yield make ILHP nanocrystal emitters very attractive for display and lighting applications. Almost all colors that were defined in 1931 by chromaticity diagram of International Commission on Illumination (CIE: Commission internationale de l'éclairage) can be exhibited by LHP nanocrystals [62-64]. This color gamut given in Figure 1.3 is wider than the ones required for LCD TV and NTSC standards [64].

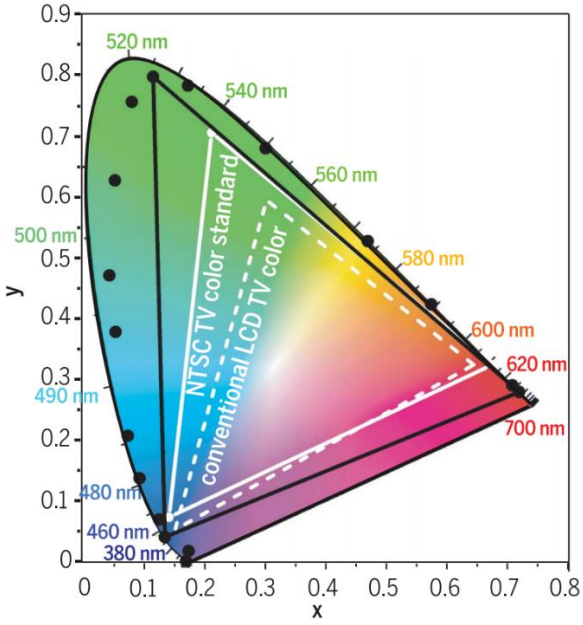

Figure 2.3: Perovskite PL spectra coordinates are mentioned with black dots [64]

2.2. Synthesis

In a typical perovskite synthesis, cesium carbonate (Cs_2CO_3) or cesium halide (CsX) salt of desired halide (X=Cl, Br, or I) is used as cesium source. The salt used for lead source is usually PbX_2 salt of desired halide. However, there are some studies getting help from lead (II) oxide (PbO) as Pb source [65]. Most of synthesis recipes involve organic ligands such as carboxylic acids and amines in favor of passivating surface defects. In addition to surface passivation, ligands help controlling the size of the crystals [67]. Oleic acid and (OA) oleylamine (OAm) are the most used ligands helping this purpose.

Selected CsX and PbX_2 salts together with surfactants are dissolved in dimethylformamide (DMF) or dimethylsulfoxide (DMSO) which are good solvents for perovskite salts. Also, there are bad solvents like toluene for mentioned salts. After a little

amount of the solution is added into a bad solvent, the good solvent releases the salts it dissolved, and solvents are dissolved in each other. Consequently, ions get together and recrystallizes as perovskite nanocrystals [66]. After centrifugation, the precipitate is dispersed in a nonpolar solvent (e.g. hexane, octane) for size-selective precipitation and ultimately obtaining pure color.

Another highly used synthesis method is hot injection where certain amount of Cs-oleate acquired from Cs_2CO_3 in octadecene (ODE) at 150°C inside a degassed flask is injected into the flask where PbX_2 salt is dissolved in a mixture of ODE, OA and OAm at a temperature higher than 120°C. After injection, the flask is submerged in an ice bath [44].

To obtain different colors, anion exchange strategy as a post-synthesis method is possible by using several salts. By changing the amount of halide anion from chloride through bromide to iodide, the color of nanocrystals can go from blue to red. This change in color can be attributed to nanocrystal size change. After nanocrystal synthesis, organic salts such as tetrabutylammonium halide, octadecylammonium halide, oleylammonium halide, etc., and lead halide salts were utilized to obtain different alloys of perovskite nanocrystals by different groups [27,31].

Shamsi discovered that applying two different ligands can control lateral sizes of perovskite nanosheets [70]. In his experiment, it was observed that different volume ratios of short to long ligands lower than 0.67 keep lateral sizes in 3nm.

In hot injection method, injection temperature was investigated by Bekenstein [68]. It was concluded that through the applied recipe, injection at 90°C results in long and thin blue nanoplates, at 130°C cyan nanoplates, at 150°C green emitting nanocubes. Higher temperatures resulted in orthorhombic nanowires and nanocubes together.

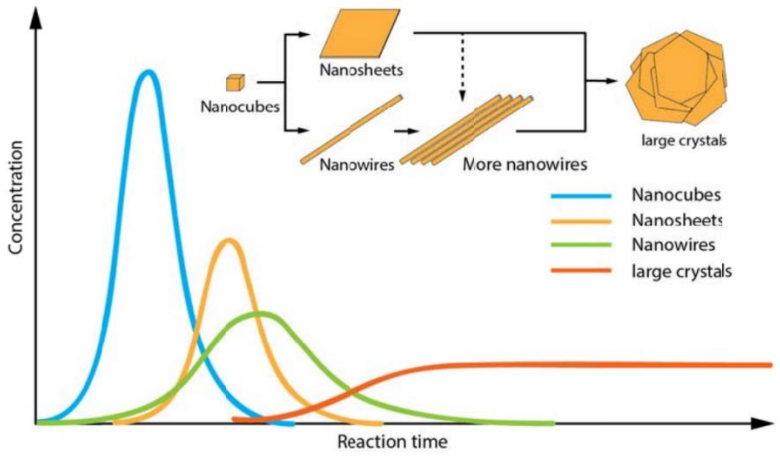

Figure 2.4: Nanostructure evolution with time [69]

The duration between quick injection of Cs-oleate and ice-bath is studied by Zhang [69]. ODE was used as the synthesis medium. 10 minutes of waiting after injection produced partly nanocubes and nanowire (as observed by Bekenstein). In 30 minutes, nanocubes, nanosheets and nanowires with uniform diameter (~10) formed. 90 minutes brought nanowires with uniform diameter (~10nm) and some big crystals that no longer exhibit quantum features. After 900 minutes crystals, as large as 0.5 μm, appeared. Thus, this study concluded that all these nanostructures evolve from each other in time. In the same study, the effect of ODE was examined for nanowire formation. The synthesis in OAm required 720 minutes to form 10-30 nm long nanowires with 60-70% quantum yield and the increase in time resulted in 10-40 nm long nanowires with 80-90% QY, which was commented as ODE is important in fast nanowire formation.

CHAPTER 3

SURFACE PLASMONS

Conduction electrons located in a metal are tended to move freely inside, which causes them to be called electron gas or electron cloud. Electrons moving near the surface of the metal determine optical features (such as absorptivity, transparency, reflectivity) of the metal. As explained by the Drude model to some extent, electrons in a metal has the opposite phase of incoming electromagnetic field, which dictates metals to have negative dielectric permittivity at the optical region. This permittivity defines shininess and color of a metal [91]. Also, the path length a field can penetrate (skin depth) into a metal is defined by the same parameter.

An electromagnetic field can interact with a metal at boundaries of that metal, where surface electrons are located. Quanta of oscillating surface electrons resulting from the electromagnetic field is called surface plasmon [72,73]. Surface plasmons can produce enormously enhanced fields very close to that surface. Their resonant condition is utilized in several applications. Surface plasmon resonance (SPR) is the case that surface electrons oscillate resonantly with incoming field. When electrons are confined in a metal nanoparticle, this situation becomes localized surface plasmon (LSP) and its resonant condition with an electromagnetic field is localized surface plasmon resonance (LSPR) which results in different consequences and is utilized in several applications. The frequency of these resonances is described by the effective mass and density of electrons, the size and shape of electron cloud and dielectric functions.

3.1. Theory

Dielectric function defines the behavior of a material under light exposure. Dielectric function for metals is defined by the Drude formula as

$$\varepsilon(\omega) = \varepsilon_{\infty} - \frac{{\Omega_p}^2}{\omega^2} \tag{3.1}$$

where ε_∞ is the converging value of dielectric constant at high frequencies, Ω_p is the plasma frequency of metal, and ω is the frequency. But this formula does not consider energy losses experienced by the metal. Plasma oscillation is observed in bulk metals due to restoring force between negative and positive charges and has a big role in plasmonic applications. Plasma frequency is given as

$$\Omega_p = \sqrt{\frac{ne^2}{m_e \varepsilon_0}} \tag{3.2}$$

where n is the density of electrons, e is the electron charge, m_e is the mass of an electron and ε_0 is the dielectric constant of free space. Most of the metals have plasma frequency in the ultraviolet regime. Electromagnetic waves with frequency higher than the plasma frequency have longer penetration depth into the metal and the metal starts to behave like a dielectric material for these waves as the difference increases. At lower frequencies, metals have high reflectivity and shorter skin depth. When losses are considered, the dielectric function of a metal is a complex function. This time, dielectric function becomes

$$\varepsilon(\omega) = 1 - \frac{{\Omega_p}^2}{\omega^2 + \gamma^2} + i\frac{\gamma {\Omega_p}^2}{\omega(\omega^2 + \gamma^2)} \tag{3.3}$$

where $\gamma=1/\tau$ is a material feature describing collision frequency of electrons, which results in energy losses, i.e. damping and τ is mean free path time of electrons. The real part of the dielectric function is responsible for the polarization, while the imaginary part for the losses. If ω and γ are compared,

$$\omega \ll \gamma, \qquad \varepsilon(\omega) \approx 1 - \frac{{\Omega_p}^2}{\gamma^2} + i\frac{{\Omega_p}^2}{\omega\gamma} \tag{3.4}$$

$$\omega \gg \gamma, \qquad \varepsilon(\omega) \approx 1 - \frac{{\Omega_p}^2}{\omega^2} + i\frac{\gamma {\Omega_p}^2}{\omega^3} \tag{3.5}$$

Since losses are inversely proportional to ω^3, high frequencies are preferred to decrease losses. But also, the excitation frequency ω needs to be lower than the plasma frequency to prevent penetration into the material and to confine plasmons between interfaces. So, when $\gamma<\omega<\Omega_p$ condition is met, it can be said to have a good plasmonic material.

The phenomenon of coupled electromagnetic waves with dipole excitations are called polaritons. Surface electron oscillations induced by electromagnetic waves are called surface plasmon polariton (SPP) or only surface plasmon. SPPs have accompanying electromagnetic waves decaying exponentially as the distance from the surface increases. In Figure 3.1 SPP propagating between metal-dielectric interface and its evanescent field amplitude as a function of the distance from the interface are shown.

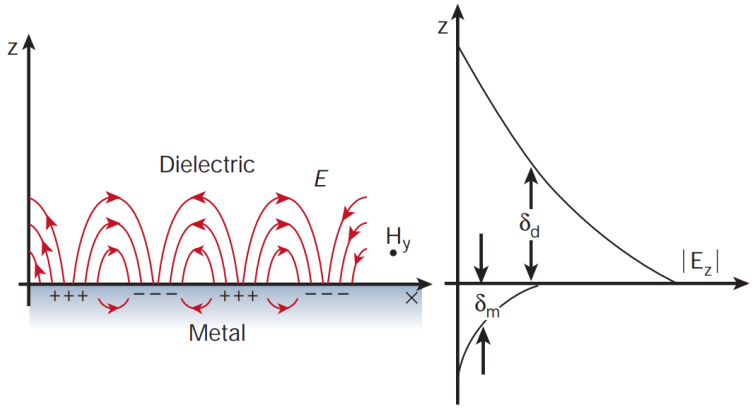

Figure 3.1: SPP propagation (left) and field amplitude (right) [75]

After Maxwell's equations are solved using metal-dielectric interface boundary conditions, one can easily see that only transverse magnetic (TM) modes survive. Under no y-dependence assumption, the electric field function of SPP propagating along x-axis is

$$E = E_0 \exp\left(i(\beta x \pm k_z z - \omega t)\right) \tag{3.6}$$

where E_0 is field amplitude, β is propagation constant of SPP (component of wavevector belonging to SPP along x direction), k_z is wavevector component along z direction and complex valued, which causes exponentially decay in z direction. The dispersion relation of corresponding SPP is

$$\beta = k_0 \sqrt{\frac{\varepsilon_m \varepsilon_d}{\varepsilon_m + \varepsilon_d}} \tag{3.7}$$

where $k_0=\omega/c$ is wavevector of light in free space, ε_m and ε_d are dielectric permittivity functions of the metal and dielectric, respectively. ε_m is a function of frequency, thus it is possible to see light and surface plasmon dispersions in the same graph:

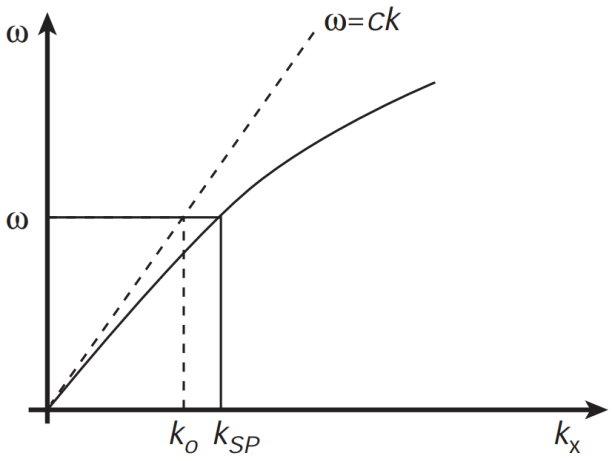

Figure 3.2: SPP dispersion relation (ksp=β) [75]

The frequency of SPPs converges to a characteristic surface plasmon frequency ω_{sp}, as the propagation constant β increases:

$$\omega_{sp} = \frac{\Omega_p}{\sqrt{1+\varepsilon_d}} \tag{3.8}$$

In order to excite surface plasmons, energy and momentum matching have to be satisfied as in SPP-light dispersion graph given in Figure 3.2. When dispersion relations of a photon and a surface plasmon are examined, it can be seen that light waves in free space do not have enough momentum to excite a surface plasmon wave at surface plasmon resonance frequency. A dielectric material which provides additional momentum to the photon is required to be used so that momentum matching is satisfied. Also as mentioned before, photons that will excite surface plasmons need to have TM polarization.

3.2. Experiment

As mentioned above, it is not possible to excite SPPs with incoming light from free space. In-plane momentum component of free space light is not sufficient to satisfy momentum matching. It is always $\beta > k_0$. In order to provide additional momentum, a dielectric material which has larger dielectric permittivity, or a grating needs to be used.

A metallic deposition having a grating section on its surface can provide required momentum to the light [78]. An electromagnetic wave sent from free space towards a metallic grating has chance to create SPP. A grating coupled SPP wavevector is

$$\beta = k_0 \sin(\theta) \pm m\frac{2\pi}{a} \tag{3.9}$$

where θ is incident angle of light onto the grating surface, *a* is spatial period of the grating and *m* is an integer. The reverse condition, where SPP is coupled to an electromagnetic radiation is also possible.

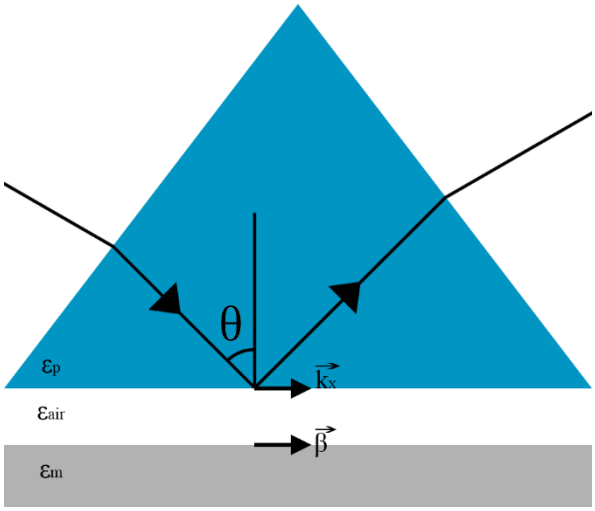

Figure 3.3: Otto configuration to excite SPPs

A configuration suggested by Otto uses a triangular prism made of glass and a spacing between the prism and the metal surface [76]. Evanescent field towards the metallic surface resulting from attenuated total internal reflection between prism-air interface has enough momentum to excite SPP in the air-metal interface. Important point here is this field is able to decay completely before reaching the metal surface. Due to the difficulty of adjusting the air gap, this configuration is not much preferred. This method transforms the dispersion relation of SPP to

$$\beta = k_0 \sqrt{\frac{\varepsilon_m}{\varepsilon_m + 1}} \tag{3.10}$$

where ε_d in the equation (3.7) is replaced by 1 since the dielectric is air. If the incident angle to the metallic surface is θ and the dielectric permittivity of the prism is ε_p, the projection of the wavevector of the evanescent field at the surface is

$$k_x = k_0 \sqrt{\varepsilon_p} \sin(\theta) \tag{3.11}$$

. When k_x is matched to β, SPP propagates along the air-metal interface.

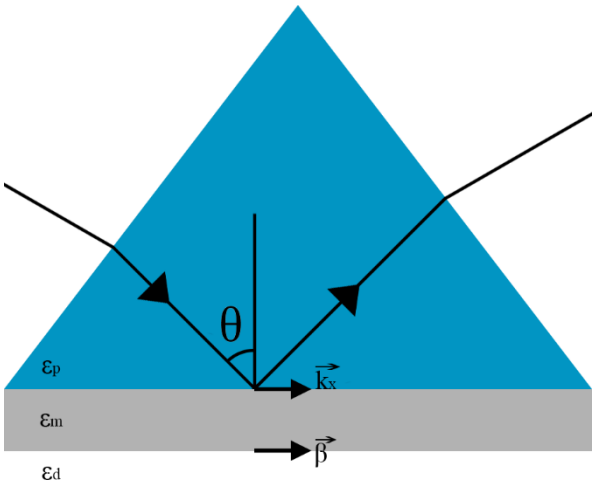

Figure 3.4: Kretschmann-Raether configuration to excite SPPs

Sometime later Kretschmann and Raether offered a new coupling technique [77]. According to the Kretschmann-Raether configuration a glass prism with one side deposited with silver can help momentum matching at the interface between the metal deposition and another dielectric material. This time the metal layer works as the spacing layer. Here, again the thickness of the spacing layer should not be so high that the evanescent field vanishes before reaching the metal-dielectric interface. As long as the momentum matching equation

$$k_x = k_0\sqrt{\varepsilon_p}\sin(\theta) = \beta = k_0\sqrt{\frac{\varepsilon_m\varepsilon_d}{\varepsilon_m + \varepsilon_d}} \tag{3.12}$$

is satisfied, SPPs are excited at the metal-dielectric interface.

3.3. SPR Applications

SPR phenomenon has been widely used in biosensor technologies to understand interactions between biomolecules since the first sensor implemented by Biacore in 1990 [98]. Detection of any biomolecule can be examined with an SPR based sensor. These sensors rely on the principle that any change in the dielectric function of the sensing surface causes SPR angle to shift.

In an SPR-based sensor, specialized metal surface (such that molecule A is immobilized on the metal surface) works as a sensor. A different molecule, say molecule B, flows over immobilized A molecules. If B attaches to A, the dielectric function of the surface changes, therefore a change in SPR resonance angle takes place (Figure 3.5). With

real-time measurements, binding efficiency, rate of association and dissociation can be determined [99].

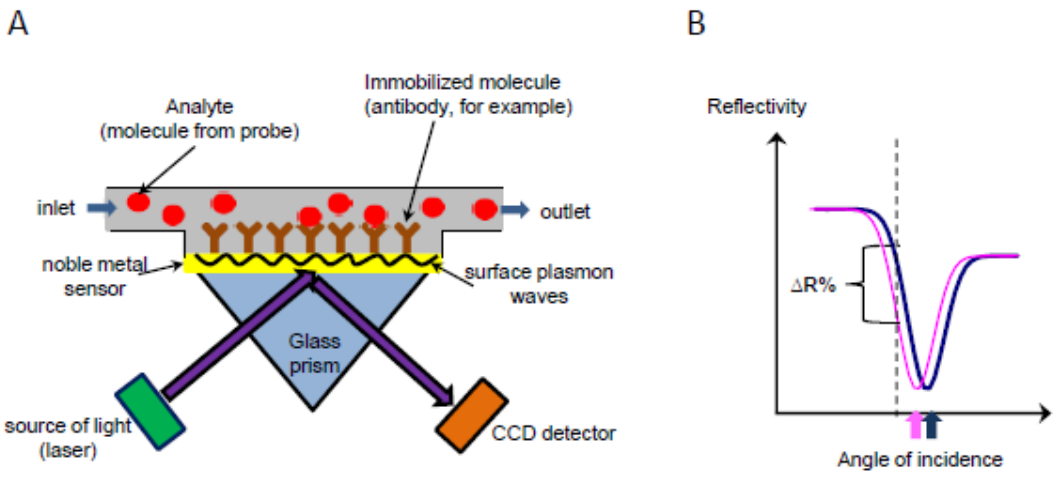

Figure 3.5: (A) SPR-based sensor schematic, (B) Change in SPR angle due to attachment [99]

3.4. Localized Surface Plasmons

Electron oscillations confined in metal nanoparticles can lead to huge field enhancement. Due to their confined nature, they have not much space to move and they are called localized surface plasmons. Their excitation, nature and outcomes are quite different from surface plasmons. Fields around metallic nanoparticles can be enhanced up to 10^8 times thanks to LSP, which is a consequence for Raman scattering enhancement. Also, fluorescence enhancement is possible with LSP coupling.

As particle size goes from bulk to nano-size, lots of characteristic features change. Gustav Mie completely solved the problem of how a metal nanosphere with radius comparable with incoming radiation behaves under an electromagnetic field exposure [79]. Nevertheless, quasi-static approximation which works for radiation wavelengths much greater than radius of the nanoparticle is sufficient to explain LSP behavior in optical regime. If the sphere radius is greater than 30nm, higher order modes like quadrupole and octupole besides dipole are able to be seen.

Skin depth of a material is a function of field wavelength. Nanoparticles with sizes comparable with skin depth of its material allow some part of the spectrum to go inside.

Therefore, the field inside the nanoparticle separates charges due to its polarization and these charges develops a restoring force. The oscillation resulting from this restoring force is related to the charge density and the effective mass of electrons inside the particle. Matching the excitation frequency with the oscillation frequency of the charges inside the nanoparticle causes strong oscillations even with low excitation field intensity. These dipoles with strong oscillations bring huge field enhancement around the particle. The field around the particle exposed to an electromagnetic field with the amplitude E_0 polarized along the x-direction is

$$\vec{E}_{out} = E_0\hat{x} - \alpha E_0\left[\frac{\hat{x}}{r^3} - \frac{3\hat{x}}{r^5}(x\hat{x} + y\hat{y} + z\hat{z})\right] \tag{3.13}$$

where α is the polarizability of the particle. While the first part of the equation is the field when there is no nanoparticle, the second part is the field given rise by oscillations inside the particle.

The damping of these oscillations can be through nonradiative or radiative decay. Nonradiative decay is due to energy dissipation, while radiative decay due to scattering [80]. Two values defined to describe these decays are absorption and scattering cross sections for nonradiative and radiative decays, respectively. However, in nano-sizes, cross sections are felt differently by every wavelength of light, and it is different from the physical cross section. Thus, it is better to define an efficiency parameter. The polarizability under quasi-static approximation, α_{qs}, determines the field profile and it is defined as

$$\alpha_{qs} = 4\pi\varepsilon_0\varepsilon_d R^3 \frac{\varepsilon_m(\omega) - \varepsilon_d}{\varepsilon_m(\omega) + 2\varepsilon_d} \tag{3.14}$$

where R is the radius of the sphere, ε_d and ε_m are the permittivity of surrounding medium and metal, respectively. The complex permittivity of the metal, ε_m, has real and imaginary parts which are functions of frequency. Effective absorption cross section which determines absorbed power to incident power flux can be calculated for a metallic nanosphere as

$$\sigma_{abs} = \frac{k}{\varepsilon_0\varepsilon_d} Im\{\alpha_{qs}\} \tag{3.15}$$

where k is the wavenumber of the external field. Effective scattering cross section which determines scattered power to incident power flux can be calculated for the same particle as follows:

$$\sigma_{scat} = \frac{k^4}{6\pi {\varepsilon_0}^2 \varepsilon_d} \left|\alpha_{qs}\right|^2 \tag{3.16}$$

By dividing effective cross section expressions with the physical cross section (πR^2), absorption and scattering efficiencies can be obtained. With a swift observation, it can be easily realized that absorption and scattering efficiencies are proportional to $1/\lambda$ and $1/\lambda^4$, respectively. Therefore, both depends on R/λ ratio. As a consequence, for small particles absorption cross section dominates the interaction. As the R/λ ratio increases, scattering rate gets much more than absorption, since scattering efficiency is proportional to R^4.

The LSPR condition can be achieved simply through considering only the polarizability, α_{qs}. Hence,

$$\varepsilon_m(\omega) = -2\varepsilon_d \tag{3.17}$$

provides the resonance if the imaginary part of ε_m is neglected, which is a good approximation for most metals of interest (Ag, Au, Al, etc.). Resonant α_{qs} leads to a huge dipole moment caused by excitation field. Consequently, the local field intensity inside and around the particle is enhanced [86].

Therefore, the LSP resonance frequency shows different values for different type of metal, size and shape of nanoparticle as well as the surrounding dielectric medium.

Electron density is the principal factor for choosing the plasmonic material. Due to the resonance condition given in equation (2.17)**,** resonance frequencies differ. Mostly, metals with higher electron density are preferred since more electrons result in stronger oscillation caused by larger polarizability [81].

Size is an important parameter manipulating decay time of the resonant interaction. Larger particles have higher damping rates [82]. Also, the larger size increases linewidth of resonance and shifts resonance to red. Larger size allows higher dipole modes to appear, which results in wider linewidth of resonance, and resonance shift to the red. Extinction cross section, the sum of absorption and scattering cross sections, defines the total interaction between the particle and light. Extinction is

dominated by absorption cross section for smaller sizes, while for larger sizes it is dominated by scattering cross section [83]. Evaluating these, one can find an ideal nanoparticle size for resonance.

The resonance is affected by shape more than size. Sphere, disc, rod, triangular or square shaped metal nanoparticles have different resonance frequency and spectrum. Particles having edges with higher curvatures show stronger field enhancement near these areas. Triangular particles have field enhancement near the corners [84]. Ellipsoids which have long, and short axes can have two different resonance peaks depending on the polarization of the external field [85]. The long axis creates resonance at a longer wavelength comparing with the one originating from the short axis. The polarization direction selects the resonance having the same direction with itself.

Dielectric permittivity of surrounding medium determines the resonance frequency as in equation (2.17). Increasing the permittivity brings longer resonance wavelength. Further, another metallic particle locating very close to the particle of interest can introduce red shift because of interaction.

3.5. LSP Coupled Emission

In previous chapters, it is explained that SPPs are seen in metallic surfaces, while LSPs are located in smaller metallic nanostructures and have different consequences. Also, there is no need of using coupling techniques to excite LSPs.

In prior studies of the literature, scientists concluded that lifetime of an excited electron is an intrinsic characteristic of an atom or a molecule. Purcell proved that this is wrong. Purcell Effect states that spontaneous emission rate of a material can be changed by external effects, which leads to a modification in luminescence [74]. This external effect can be chosen to be surface plasmons of a metallic nanoparticle. Any luminescent material brought close to a metallic structure is affected by quenching or enhancement of emission under certain conditions.

Emission of a fluorescent material can be enhanced near a metallic nanoparticle by tailoring the distance between the emissive and metallic particles. While very small distances cause quenching due to energy transfer from emitter to metal nanoparticle, enhancement takes place in larger distances which can be obtained by placing a dielectric spacer between them. If the emission peak of the emissive material coincides with the

absorption peak of the plasmonic structure, the enhancement occurs as long as there is a certain distance between them.

The rate of fluorescent emission γ_{fl} is given by

$$\gamma_{fl} = \gamma_{exc} \cdot \eta \tag{3.18}$$

where γ_{exc} is excitation rate (probability of getting the electron to the excited state), η is quantum yield. Quantum yield is the ratio of radiative decay rate and all decay rates combined (ratio of emitting a photon over all emissions) and is defined as

$$\eta = \frac{\gamma_{rad}}{\gamma_{rad} + \gamma_{nrad} + \gamma_{int}} \tag{3.19}$$

where γ_{rad} and γ_{nrad} are radiative and nonradiative decay rates, respectively. γ_{int} is intrinsic nonradiative decay rate of excited electrons. Phonon emission or reabsorption rates can be counted in this intrinsic rate and γ_{int} can be neglected for efficient emission sources since γ_{rad} is high. In vacuum, γ_{nrad} has no impact, therefore intrinsic quantum yield η_0 is

$$\eta_0 = \frac{\gamma^0_{rad}}{\gamma^0_{rad} + \gamma_{int}} \tag{3.20}$$

where γ^0_{rad} is radiative decay rate in vacuum. In the light of (3.18), (3.19) and (3.20), fluorescent emission rate enhancement Q_F is possible to be obtained:

$$Q_F = \frac{\gamma_{fl}}{\gamma^0_{fl}} = \frac{\gamma_{exc} \cdot \eta}{\gamma^0_{exc} \cdot \eta_0} = \frac{\gamma_{exc}}{\gamma^0_{exc}} \cdot \frac{\gamma_{rad}}{\gamma^0_{rad}} \cdot \frac{\gamma^0_{rad} + \gamma_{int}}{\gamma_{rad} + \gamma_{nrad} + \gamma_{int}} \approx \frac{\gamma_{exc}}{\gamma^0_{exc}} \cdot \eta \tag{3.21}$$

In equation (3.21), γ_{int} is neglected. Consequently, (3.21) tells that the excitation rate which is proportional to the fluorescent emission rate can be enhanced with external effects. But as mentioned previously, the distance of the fluorescent to the metal particle should be tuned in order to see enhancement.

In 2006, Novotny reported experimental and theoretical study of quenching and enhancement [87]. They used 20, 60, 80 and 100 nm diameter gold spheres to investigate the distance factor on fluorescence emission rate, theoretically. Radiative emission rate enhancement increases as the metallic particle got closer, but after a maximum enhancement distance, fluorescent emission quenches rapidly. For 20 nm gold particle, no enhancement is expected, however quenching occurs for distances shorter than a certain amount. Reason of quenching was explained such that quantum yield decreases faster than the increasing speed of excitation rate as the distance decreases [97]. Attaching an 80 nm gold particle at the end of a fiber, and controlling its position accurately, they

examined the effect of distance on a single molecule and obtained consistent results with the theory.

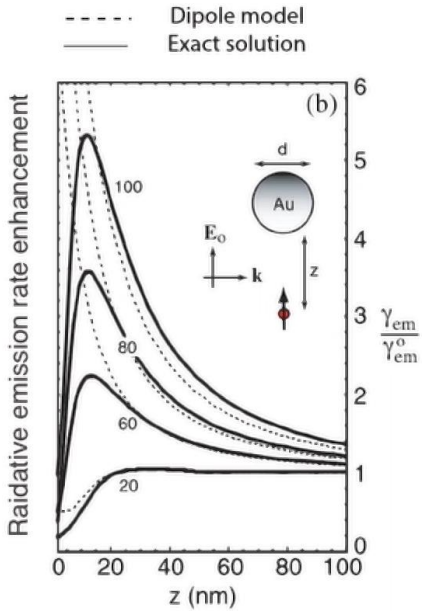

Figure 3.6: Effect of gold nanoparticles with diameter d and z nm distant from fluorescent material on the radiative emission rate [87]

LSP coupled emission has some advantages over SPP coupled emission, such that LSPR frequency is adjustable with type, size, geometry and interparticle distance of metal nanoparticles and due to confinement and not being able to propagate long distances, energy loss is less [92].

3.6. Fabrication Methods of LSP Sources

LSP requires metallic nanoparticles. It is possible to fabricate metallic nanoparticles through vacuum deposition, electron beam lithography (EBL), nanosphere lithography or chemical synthesis.

Vacuum deposition is a facile way to produce metallic nanoisland films that exhibit localized surface plasmon properties. After deposition, thermal annealing can help tune LSPR frequency. Annealing at different temperatures for different durations changes peak absorption wavelength by controlling nanoisland size and height [93].

In order to fabricate certain nanoparticle shapes with high resolution, EBL is a rich and precise method. Steps for producing desired structure in EBL is given in Figure 3.6(a) [94]. Pompa et al. fabricated an array of triangular gold prisms by EBL and these

structures showed LSP source feature [95]. Disadvantages are the cost of equipment and the difficulty of scaled-up production over large areas.

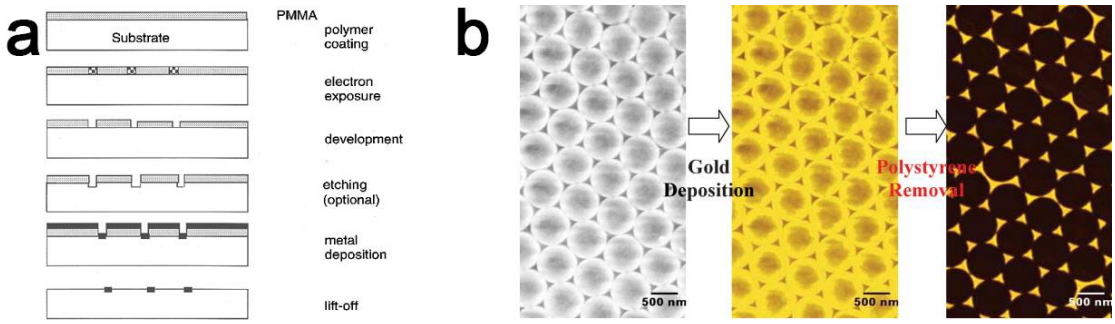

Figure 3.7: (a)EBL steps [94], (b) Nanosphere lithography process [96]

Nanosphere lithography utilizes a solution containing nanospheres that will work as a mask for vacuum or electron beam deposition [96]. Hexagonally closely packed spheres allow triangular areas among every three adjacent spheres to be filled with metal nanoparticles during deposition. After removal of nanospheres, metallic triangular nanoparticles that will serve as LSP sources are obtained. Corners of the nanotriangles exhibit strong collective electron oscillations which are useful for field enhancement. However, obtaining different shapes than triangles is difficult.

CHAPTER 4

EXPERIMENTAL METHODS

4.1. Physical Vapor Deposition

It is possible to produce metal nanoisland films by using physical vapor deposition in order to achieve LSP resonance. Physical vapor deposition (PVD) is a method of thin film deposition. Some PVD techniques are thermal evaporation, electron beam (e-beam) evaporation, reactive and activated reactive electron beam evaporation, sputtering, filtered cathodic arc deposition, ion plating, pulsed laser deposition. We used thermal evaporation chamber in the glovebox within the body of IZTECH Photonics Laboratory.

4.1.1. Mechanism of Thermal Evaporation

This technique is based on heating the source material resistively in a vacuum chamber. The reason of vacuum requirement is to benefit from facilitation of vaporization under vacuum, and to prevent interaction with floating particles. A large current is applied through the boat (a thermally tolerant material, usually made of tungsten) in which the source material is held. Electrical resistivity of the boat generates heat resulting in evaporation of the source material. The vapor of the material travels randomly through the high vacuum chamber. When reached on a surface, it condenses and constructs a film. A schematic of a PVD chamber is given in Figure 4.1.

The sample to be deposited face downward above the source material. Before deposition, after samples are placed, a rough pump in the chamber reduces pressure to 1 mBar. At this value, a turbomolecular pump gets activated and starts to evacuate even faster. 10^{-6} mBar is sufficiently low pressure to evaporate most metals. User controls current that passes through the Tungsten boat. When enough heat is attained through electricity, evaporation begins, and the vaporized material moves randomly in the chamber. A shutter placed between the sample and the source prevents deposition on the samples in the beginning. The current flowing through the boat is varied to obtain a desired rate, which is measured by a quartz crystal microbalance (QCM) sensor. After reaching a target rate, the shutter is opened, and deposition starts. Thin film thickness is characterized by the deposition rate and deposition time. The movable shield (shutter) is

restored as the thickness arrives at the aimed value. Current flow is slowly decreased to stop evaporation. Chamber is refilled and samples are taken out.

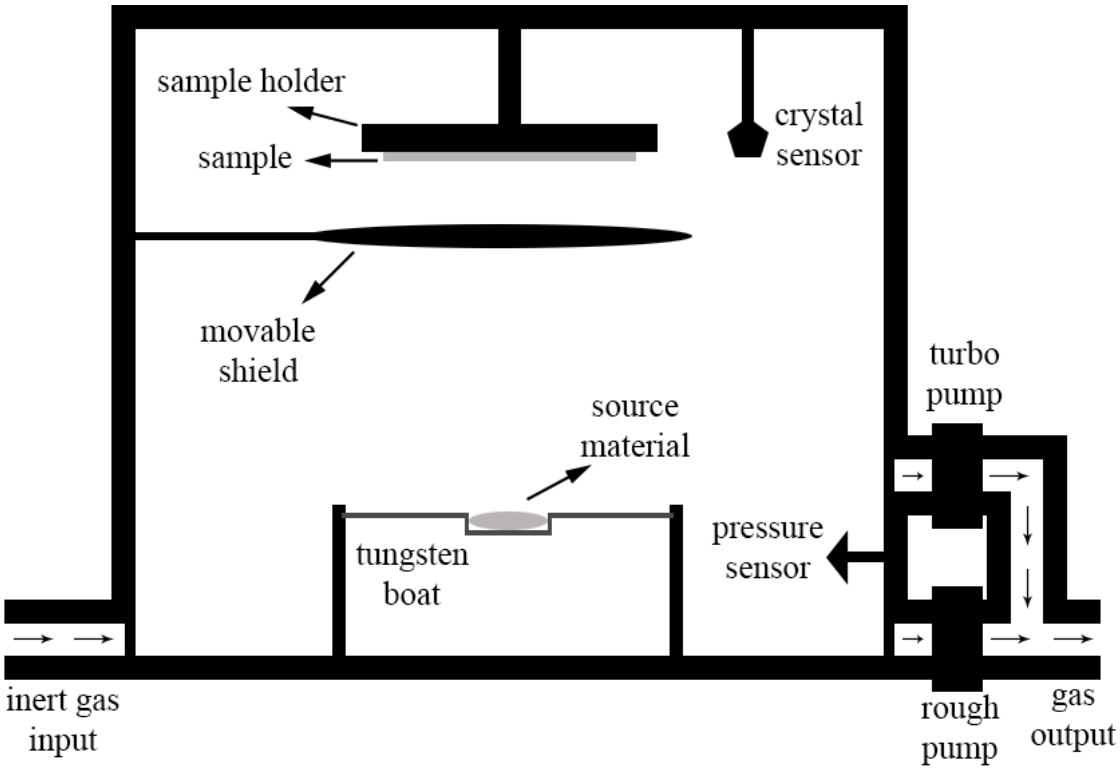

Figure 4.1: Thermal evaporation chamber

Advantages of thermal evaporation are:

- Simple and cheap,
- Less surface damage,
- Perfect film purity.

Readers interested in more details about PVD techniques are suggested to consult in references [88] and [89].

4.2. Atomic Layer Deposition

Atomic layer deposition (ALD) is the process that after every cycle one lattice thick layer of a material is being grown on a substrate or sublayer. It is also known as atomic layer epitaxy. This method enables its user to obtain very precise layer thicknesses. Thanks to its good reproducibility, it is a widely preferred technique when uniform layers are needed. In this thesis study, ALD is utilized to obtain Al_2O_3 layers in various thicknesses.

During our experiments, ALD Cambridge Nanotech Savannah S100 located in the clean room of Bilkent University UNAM was used.

4.2.1. Working Principle of ALD

The ALD chamber has one gas input hole and one vacuum output hole both looking upwards, between which samples are placed. After samples are settled in the ALD chamber, the chamber is vacuumed, and the temperature is increased to a desired degree. Since the deposition temperature has the ability to change the layer thickness after each cycle as a result of changing bond lengths (temperature-bond length table is given in the table below), the temperature needs to be stable as long as the process continues.

Before the deposition, the samples are already affected by water molecules because of the ambient conditions, that is H_2O molecules in air decomposes to their hydroxyl groups, and their adsorption to the substrate establishes a favorable setting for ALD process.

After obtaining vacuum and constant temperature, a pulse of trimethylaluminum ($Al(CH_3)_3$ a.k.a. TMA) gas is sent to the chamber and it flows over samples. TMA molecule and a hydroxyl group adsorbed on the sample surface interact, leading to methane (CH_4) gas formation, while aluminum with its remaining two methyl groups bonds to an oxygen atom which lost its hydrogen to a methane molecule (Figure 4.2-3). Other than Al_2O_3, one might want to use a different material to deposit. Then, the only change will be the precursors such as:

- diethylzinc ($(CH_3)_2Zn$) for ZnO,
- tetrakis(dimethylamido)titanium ($Ti(NMe_2)_4$) for TiO_2,
- tetrakis(dimethylamido)hafnium ($Hf(NMe_2)_4$) for HfO_2.

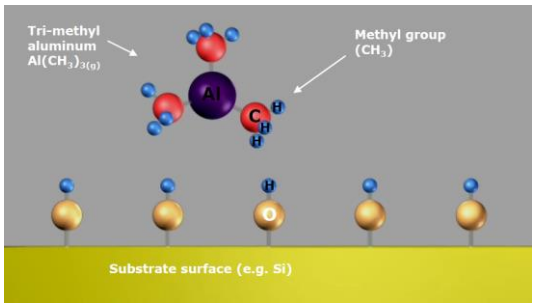

Figure 4.2: TMA is sent to the ALD chamber

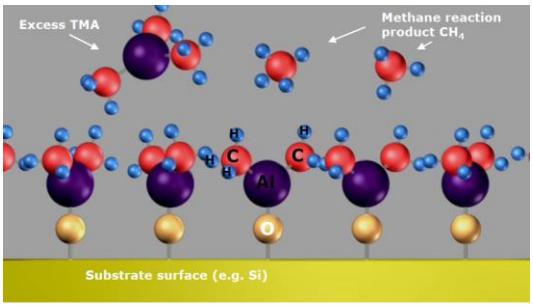

Figure 4.3: TMA molecules bond to O atoms and extract CH4

Next step to waiting for excess products (excess TMA, H_2O, CH_4) to leave the chamber is to send a pulse of pure water (Figure 4.4). The oxygen in a water molecule gives its hydrogens to each remaining methyl groups of Al. At the end, the by-product is methane, again. While Al atoms are holding each other via O atoms, every Al has got a hydroxyl group towards the surface direction as in the beginning, establishing an infrastructure for future layers (Figure 4.5). Consequently, a layer consisting of 2 Al and 3 O atoms is formed (Figure 4.6). The representation of a layer consisting of three layers is given in Figure 4.7.

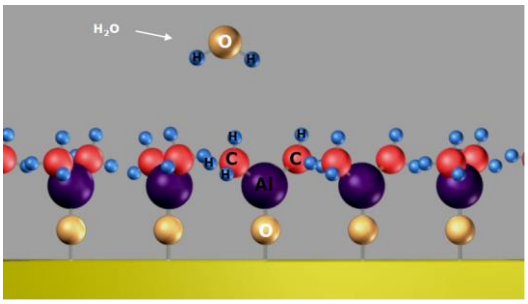

Figure 4.4: H_2O enters the chamber

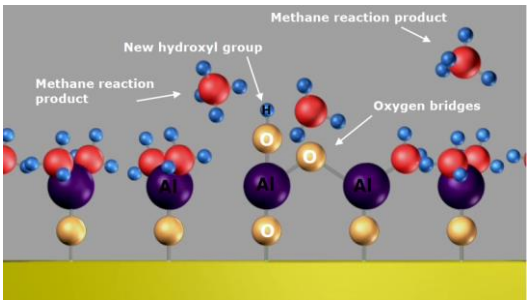

Figure 4.5: By-product CH_4 molecules leave while new hydroxyl groups and O bridges between aluminum atoms are forming.

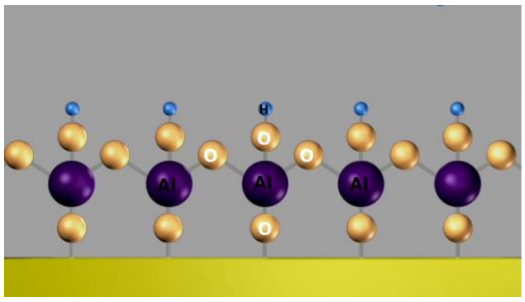

Figure 4.6: One layer of Al_2O_3 with its hydroxyl group

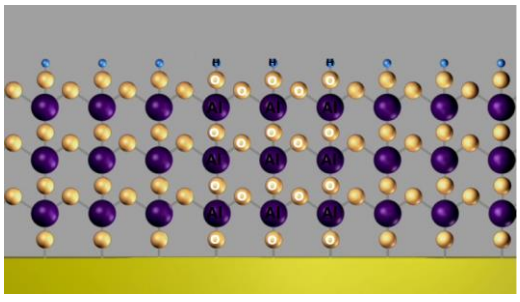

Figure 4.7: 3 layers of Al_2O_3

Some of obtained thickness values by the manufacturer for different precursors at different temperatures are given in the table below.

	Al_2O_3	**ZnO**	**TiO_2**	**HfO_2**
80°C		1.25-1.3Å/cycle		
150°C	1.04Å/cycle		0.40Å/cycle	
200°C	1.05Å/cycle	1.46Å/cycle	0.40Å/cycle	1.01Å/cycle
250°C	1.06Å/cycle		0.39Å/cycle	
300°C	1.08Å/cycle			

Table 4.1: Layer thickness for different temperatures and materials

4.3. Scanning Electron Microscopy

A scanning electron microscope (SEM) is a microscope that focuses and scans electrons instead of light on the contrary of traditional optical microscopes in order to get a display of a sample. Interaction of these focused electrons create various signals that are collected by detectors to get knowledge about the surface of a sample. Quantity of electrons coming out of every scanned unit area determines the contrast of the pixel of the picture that created on the computer screen. In conclusion, user sees a black-and-white image of the sample surface.

Visible wavelengths differ from 400nm to 700nm. If the average wavelength is accepted for our calculations, theoretical limit of sample visibility of an optical microscope is about ~275nm. To see beyond this size, it is restricted to use a wavelength shorter than this limit. Electrons give opportunity to overcome the limit and see smaller sizes with their smaller wavelength.

In our SEM analyzes, FEI Quanta 250 FEG SEM within the body of Integrated Research Centers (TAM) in IZTECH was used.

4.3.1. Working Principle of SEM

An optical microscope and a SEM consist of components which have very similar tasks but are of different structures (Figure 4.8). Main SEM parts are specimen chamber,

vacuum system, electron gun, column, detectors, imaging system and water chilling system.

Samples are placed in the specimen chamber of SEM. When enough vacuum is reached, samples are ready to be observed. Vacuum is needed to prevent scattering of electrons by gas molecules before they reach the sample. A SEM may have two vacuum modes: high and low. Depending on the specimen type (e.g., biological, solid state, etc.) some specimens can be seen better at one of these modes, while worse at the other.

Electron gun, a filament on the ceiling of the specimen chamber, produces electrons and shoots them towards samples at a speed. The speed of electrons is controlled by voltage. The higher the voltage is, the faster the electrons are. This speed and the density of the sample determine how deep electrons can penetrate the sample. Areas containing higher atomic number elements produces brighter pixels on the computer screen since source electrons interact higher number of electrons, comparing with areas with elements of lower atomic number do.

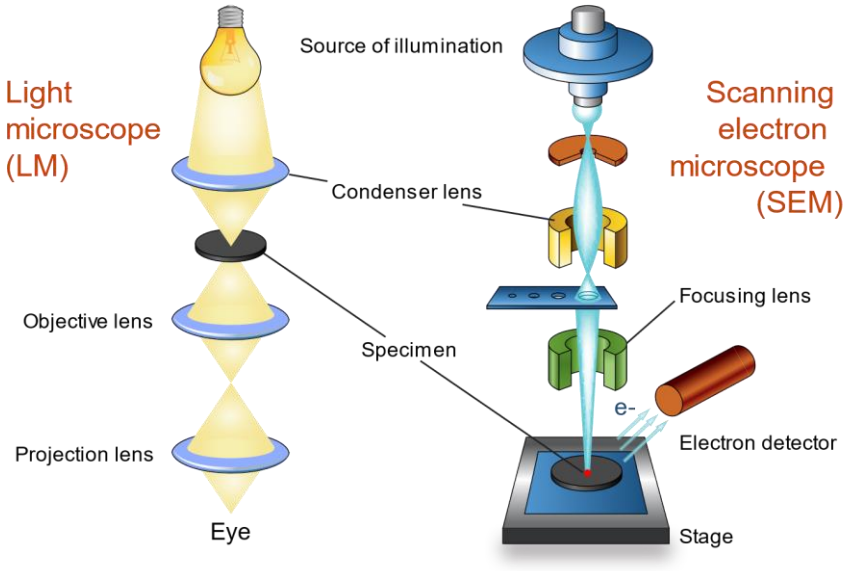

Figure 4.8: Comparison of SEM with an optical microscope [35]

Until electrons interact with the specimen, they pass through some electron lenses and apertures for the width and therefore, spot size of electron beam to be controlled. Electron movement can be controlled by a magnetic field which is provided by magnetic lenses in the column. Magnetic field causes electrons to follow a helical path downwards, as shown in Figure 4.9. Altering the current flowing through the coil, focal length is changed. The condenser lens changes the intensity falling onto the sample. The objective

lens provides focusing. Scan coils placed above the objective lens maintains scanning over the sample to get complete image of the desired area.

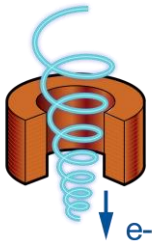

Figure 4.9: Helical path of electrons [35]

Electrons hitting on the surface produce secondary electrons, backscattered electrons, and characteristic X-rays, all of which has a different detector type. Backscattered electrons are electrons that bounce back after hitting the sample. These are collected by backscattered electron (BSE) detector. Electrons removed from the sample after the impact of source electrons are called secondary electrons and gathered by secondary electron (SE) detector. As conclusions of these interactions, X-rays, light or heat are radiated (Figure 4.10). The detector for energy dispersive X-ray spectrometry (EDX or EDS) catches X-rays to inform the user about the containing of the sample. Only SE detector requires high vacuum. Both other detectors can work under low vacuum.

As demonstrated in the Figure 4.10, SE detector gathers information from the specimen surface. SEs, as low energy electrons, requires SE detector is closer to the sample than BSE detector. SEs are good tool to understand the topology. On the other hand, BSE detector collects higher energy electrons and obtains information about subsurface.

Images the user see differs according to the spot size. Large spot spans areas via larger points, thus the source of the pixel created on the computer screen is from a large area. That means the user is not able to see details of the specimen. In Figure 4.11 the topology perceived by the user is demonstrated by the scan line.

SEM also needs 20°C temperature for its magnetic lenses to work properly. There is also a feedback mechanism for the cooler: If it fails and lenses get hotter than the normal, SEM shuts itself down.

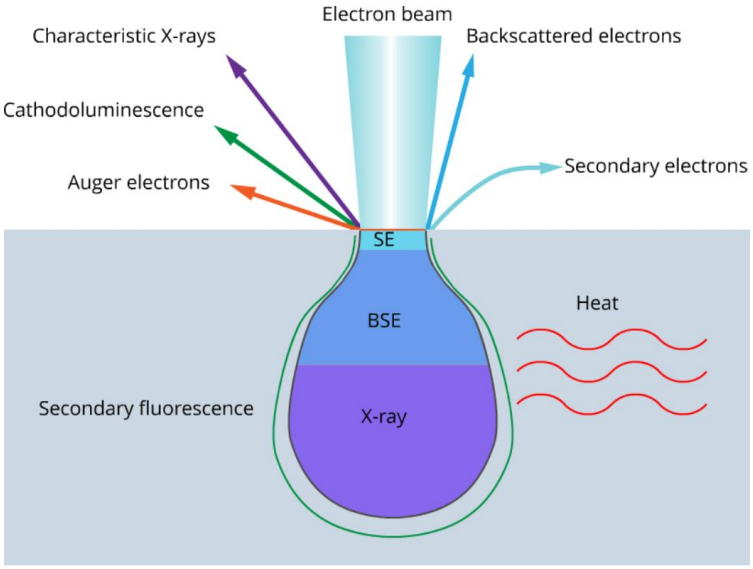

Figure 4.10: Source electrons - sample interaction [35]

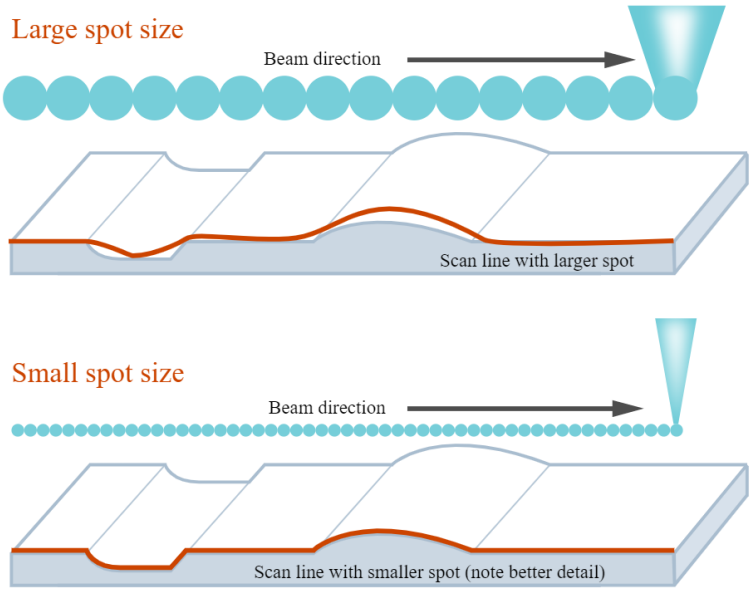

Figure 4.11: Spot size comparison [35]

4.4. Optical Spectroscopy

In pursuance of characterization of samples, transmission, absorption, photoluminescence (PL) and time-resolved photoluminescence (TRPL) measurements were carried out. The measurement device for all these analyses were Edinburgh FS5 Spectrofluorometer of IZTECH Laboratories. The device has 150W Xenon arc lamp.

Light sources made of xenon can present every visible color, which makes them a reliable candidate for representation of the Sun. A spectrum comparison for the Sun, a xenon arc lamp and a metal halide lamp are given in Figure 4.12.

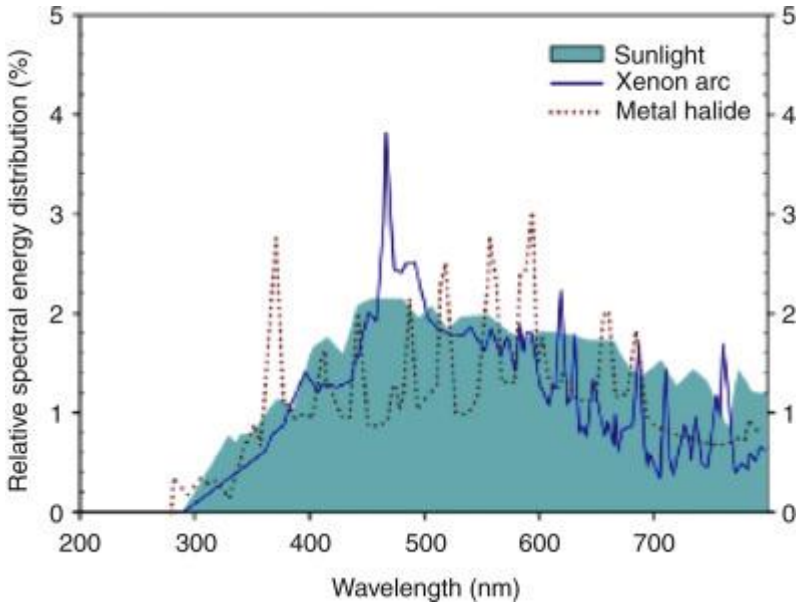

Figure 4.12: Sun, xenon arc and metal halide lamp spectrums [90]

4.4.1. Photoluminescence

The process of emitting photon as a result of photonic excitation of a material is called photoluminescence. PL measurement schematic is given in Figure 4.13.

PL measurement requires shorter wavelengths than the emission wavelength of a material. Since ultraviolet (UV) light has longer wavelength and higher energy than the visible spectrum has, usually an ultraviolet wavelength is used to see a visible emission.

In a PL setup, photons coming out of a light source visits a monochromator to eliminate photons with undesired wavelengths. Light having the desired wavelength passes through a tunable slit to tune its bandwidth. Source light hits the sample and the sample emits new photons with lower energies. The emission bandwidth is controlled by another (exit) slit. Another monochromator placed before a photodetector array to measure intensity of incoming light for every wavelength. The photodetector catches these photons and a computer makes a histogram for every wavelength.

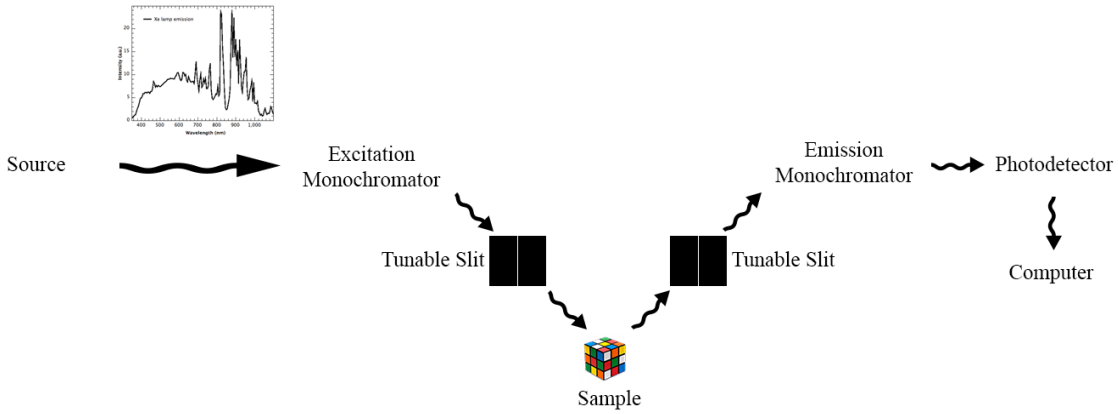

Figure 4.13: Photoluminescence measurement schematic

4.4.2. Transmission

Transmission measurement is useful to determine a materials transparency feature for different wavelengths. In a typical transparency measurement, the sample is placed between an excitation source and a detector. An excitation monochromator picks wavelengths as in PL measurement. A photodetector collects photons passing through the sample. According to the intensity of light gathered by the photodetector, a histogram is created by a computer to see how much light is transmitted for which wavelength. A simplified transmission measurement setup is given in Figure 4.14.

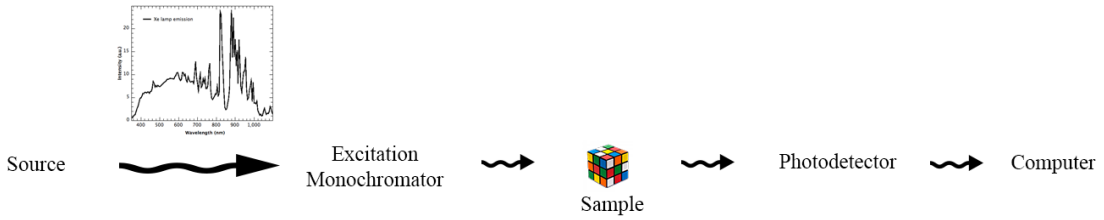

Figure 4.14: Transmission measurement schematic

Transmission information is typically given in percentages. Thus, the quantity of light produced by the source has to be known. If the measurement can be done without a sample and the result taken from the sample is divided by the result with the sample, percentage information for every wavelength can be obtained.

4.4.3. Absorption

An absorption measurement requires subsequent transmission measurements. To measure how much light is absorbed, one need to know how much light is produced by the source. As in the transmission measurement, if the measurements with and without the sample are implemented, absorption information can be extracted. The difference of the results of these two measurements give the absorption data. Again, percentage can be calculated by the ratio of this data to the result of no sample data.

4.4.4. Time Resolved Photoluminescence

Decay rate of a material's excited electrons are evaluated by a time resolved photoluminescence (TRPL) (or time correlated single photon counting (TCSPC)) setup. A pulsed laser source is obliged to excite electrons in a TRPL setup. After each pulse, with the help of a fast photomultiplier tube (PMT) detector, a computer counts photons and creates a histogram for every time point the detector catches photons. After the fitting of this histogram to a multi- or mono-exponential function, decay rates are found by using time constants of this function.

The off time of the pulse period of the laser must be longer than inverse decay rate, lifetime, of electrons. Otherwise, most of the excited electrons stay excited when a new pulse of the laser is sent. This situation does not give enough information to obtain the lifetime.

4.5. Atomic Force Microscopy

Atomic force microscopy (AFM) is used to figure out the surface topology of a specimen. At the bottom surface of a cantilever, a needle touching or hovering over a surface describes how rough, wavy, inclined, or smooth the sample is.

An AFM has three modes of operation: contact mode, tapping mode, and non-contact mode. Contact mode makes the needle almost touch the surface to create surface data. Tapping mode makes the needle do an oscillatory motion and the tip of the needle almost touch the surface at its lowest point of oscillation. This mode prevents breakdown of the needle when the surface roughness is high. The needle does not get so close as in the other modes in non-contact mode, but it makes an oscillatory motion, too.

Owing to roughness of silver surfaces deposited via thermal deposition in this study, tapping mode of operation is used to define surface roughness and average layer thickness of silver films.

4.5.1. AFM / Tapping Mode

The cantilever's oscillating motion with the amplitude changing between 20 - 100 nm gathers surface information from the sample. This oscillation is very close to the resonant frequency of the cantilever. At the minimum point of the oscillation, the needle touches softly, taps on, the sample. The vibration frequency changes upon this contact. The deviation from the resonant frequency defines the height on that point.

Tapping mode averts forces related to the tip of the needle, which can damage the sample surface and is useful for weak structures. Image resolution changes due to tip diameter of the needle. Smaller diameter tips give higher detailed images.

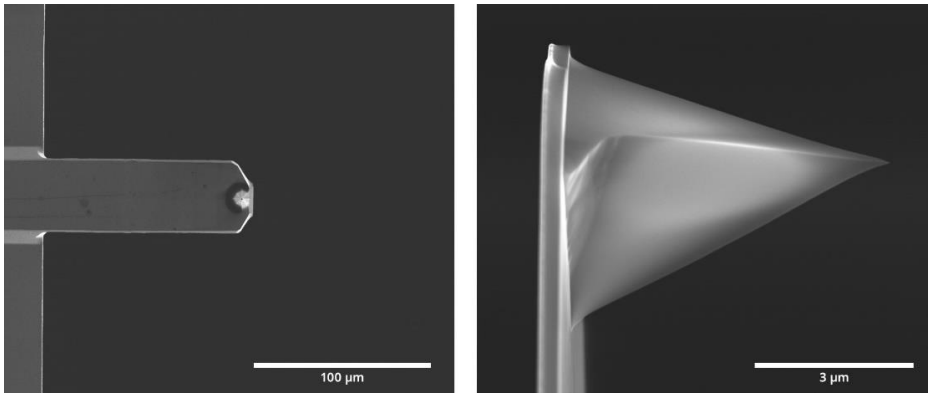

Figure 4.15: Optical and SEM images of an AFM tapping mode needle [35]

4.6. Perovskite Nanowire Synthesis

Perovskite nanowires were synthesized by adapting Daniel Amgar, et al.'s tunable length perovskite recipe [36].

According to this method, Cs-oleate synthesis was implemented in a 50 mL 2-neck flask. 0.4 g Cs_2CO_3 and 1.25 mL OA were added into 15 mL of ODE. Then, this mixture waited for 1 hour at 120°C to be degassed. Later providing N_2 atmosphere inside the flask, the temperature was increased to 150°C and waited for 1 hour to obtain Cs-oleate.

$PbBr_2$ precursor was acquired by solving 0.735 gr of $PbBr_2$ in 5 mL of DMF inside a 20 mL glass vial. This solution heated for 1 hour at 80°C. In order to get rid of undissolved excess $PbBr_2$, the solution was filtered with a 0.22 μm filter.

For nanowire formation a different 20 mL glass vial which was called reaction vial was used. 0.125 mL of OA, 0.125 mL of OAm and 1.25 mL of ODE were mixed in the reaction vial. Firstly, 0.1 mL of Cs-oleate precursor was added to the reaction vial. Later 0.2 mL of $PbBr_2$ precursor was added. After 10 seconds of stirring, 5 mL of acetone added. The solution color became turbid white and slowly turned to green. Acetone provided the crystallization of nanowires. The total $CsPbBr_3$ nanowire solution was about 6.5 mL. This solution divided to six 1 mL centrifuge cases. To collect precipitate nanowires, centrifuge cases were centrifugated at 3000 rpm for 5 minutes. The supernatant solution which involves DMF, acetone, and other excess materials pipetted out. Over the precipitate, 1 mL of hexane were added into each case to disperse nanowires. After one more centrifugation at 3000 rpm for 5 minutes, supernatant $CsPbBr_3$ nanowires dispersed in hexane were collected from each centrifuge case to a new 20 mL glass vial and sealed and kept in a fridge for further usage.

CHAPTER 5

EXPERIMENTAL RESULTS

Our experiment was consisting of 3 parts: nanowire synthesis, plasmonic layer deposition and combining both of them.

As mentioned in the section 4.6, perovskite synthesis recipe from the reference [36] is used. In our experiments, we realized that by changing the reaction vial, $PbBr_2$-precursor and Cs-oleate precursor temperatures it is possible to change synthesis yield, PLQY and peak emission wavelength. After discovering that, we decided to shift the peak emission a little further than the original synthesis which gives peak emission at ~455nm.

The second part of the experiment was finding a proper thickness for plasmonic layer. Silver nanoisland layers in several thicknesses were annealed for different times and their absorption characteristics were compared. The one with the best absorption intensity was picked in order to obtain a strong resonance. Also, the peak of absorption belonging to the selected sample was at a lower wavelength than the peak emission wavelength of nanowires, so that after the dielectric spacer deposition peaks could match.

At the last part, nanowires were spin coated over Ag nanoisland-Al_2O_3 complex. For every dielectric layer thickness, PL and TRPL measurements were implemented to see enhancement and lifetime changes.

For PL, TRPL, PLQY and absorption measurements, Xenon arc lamp was used as excitation source. Xenon arc lamp spectrum is given in Figure 5.1.

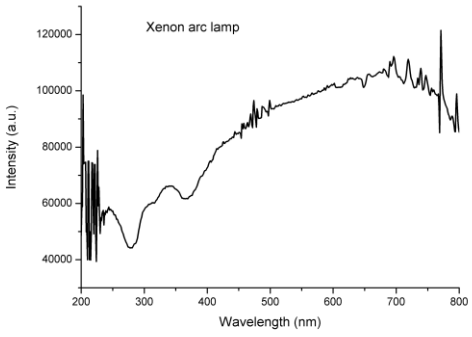

Figure 5.1: Xenon lamp emission spectrum

5.1. Nanowire Synthesis

Precursor temperature has high influence on synthesis. It is concluded that Cs-oleate precursor temperature has effect on only emission intensity of nanowires. Keeping the reaction vial (involving 1.25 mL ODE, 0.125 mL OA and 0.125 mL OAm) and $PbBr_2$ precursor at room temperature while using Cs-oleate at different temperatures, it was observed that emission intensity got higher for higher temperatures. The emission characteristics of nanowires synthesized with Cs-oleate at 100°C, 125°C and 150°C are given in Figure 5.2. PL peaks located at 456-457 nm.

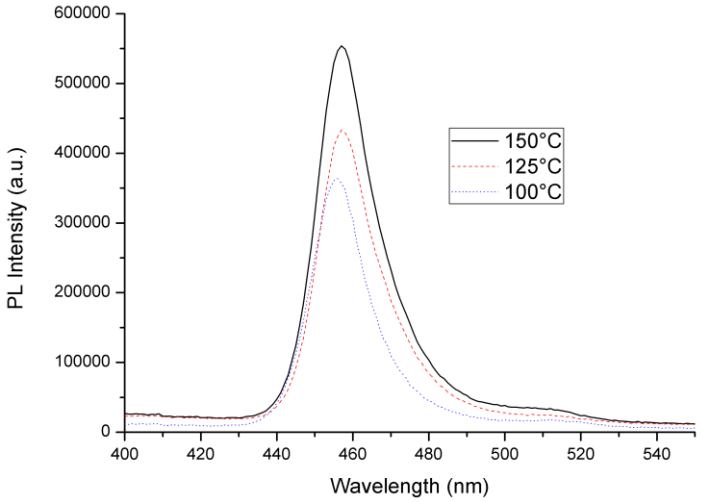

Figure 5.2: PL of nanowires synthesized with Cs-oleate at 100°C, 125°C and 150°C

Different temperatures of reaction vial (RV) and $PbBr_2$-precursor resulted in double peaked emissions, which is not useful for plasmonic enhancement investigation.

However, using RV and $PbBr_2$-precursor at the same temperature caused a red shift in peak. Normalized PL for synthesis at RT, 70°C and 85°C are given in Figure 5.3.

Perovskites are well-known for their degradation with time and ambient conditions. This was tested with the same perovskite precursor. The same amount of perovskite precursor solution was deposited on glass. One of them kept in glovebox and one under ambient conditions. One week later, a new deposition was done, and measurements were taken. Decrease in PL intensity was experienced for both of depositions which were made one week before. But ambient conditions influenced perovskites more harshly. Results for these observations are given in Figure 5.4.

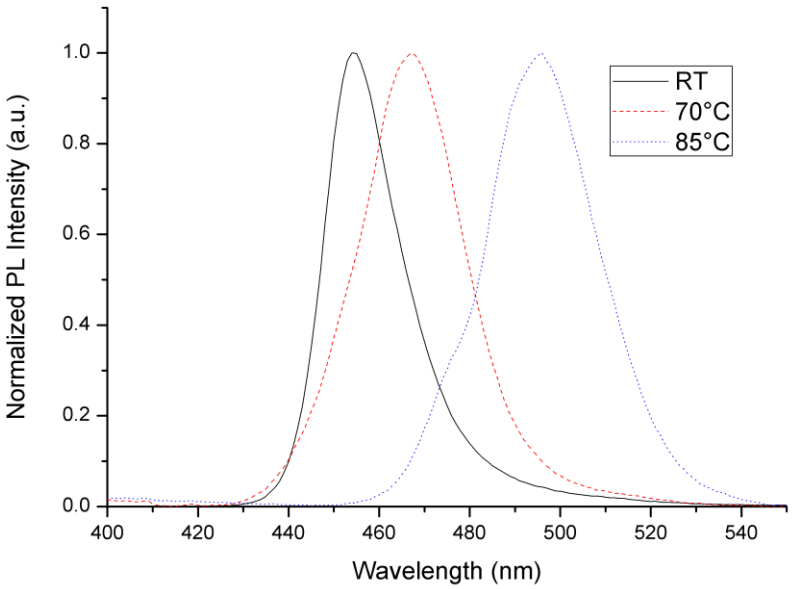

Figure 5.3: PL for RV and $PbBr_2$-precursors at RT, 70°C and 85°C

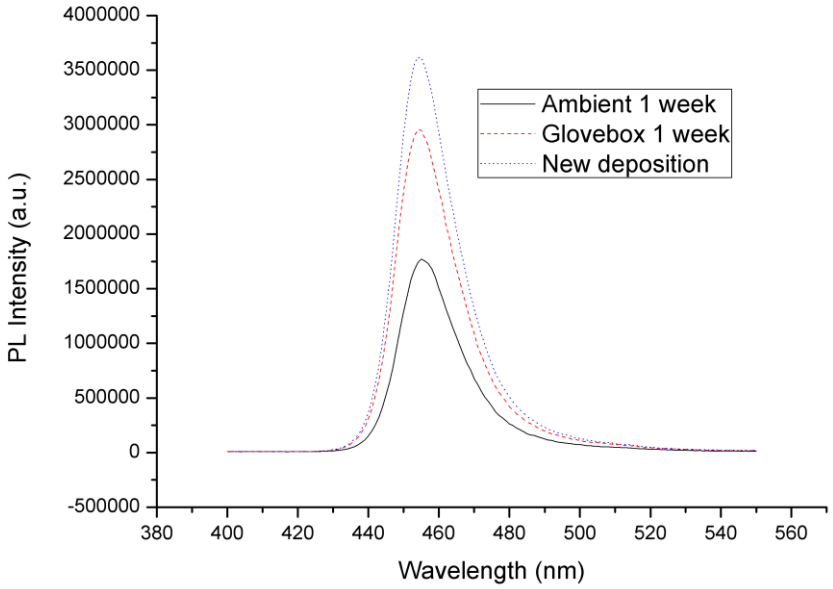

Figure 5.4: PL intensity degradation with time and conditions

5.2. Plasmonic Layer Fabrication

To observe LSPR effect, sharp edges in nano-sizes are useful. Therefore, nanoislands which have steep peaks were chosen as plasmonic layer. Thermal evaporation (mentioned in Section 4.1) is a facile way to fabricate a nanoisland layer.

First step was to choose a metal to serve as plasmon source. Gold has absorption peak wavelength way farther than our nanowire's PL peak. Thus, it was not suitable for our purpose. On the other hand, silver has a peak absorption which is towards blue side of the spectrum and it is a renowned plasmonic material for enhancement purposes. For this reason, silver was selected.

Silver layer thickness determines the plasmonic behavior. If it is too thick, plasmonic effects can vanish since the electron confinement will be terminated. After a suitable thickness is picked, a careful engineering to tune the absorption peak is needed.

Accordingly, silver nanoisland layers were deposited on glass substrates. Deposition rate was kept as 0.1 Å/s so that nanoislands can be distinguishable in order to see more LSPs [100]. To find an acceptable absorption feature, several nanometers of silver was deposited and annealed for different durations. Obtained results are discussed in the following paragraphs.

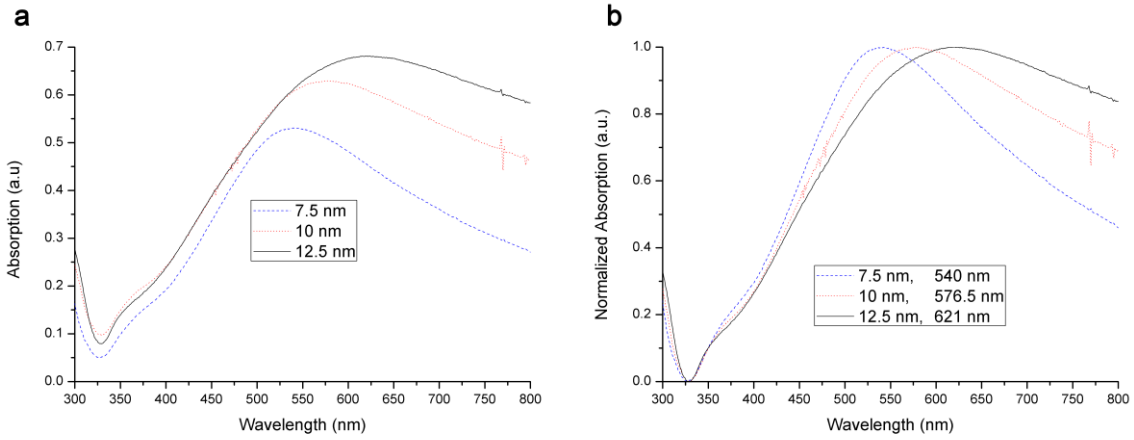

Figure 5.5: For 7.5nm, 10nm and 12.5nm silver nanoisland layer a) absorption spectrum and b) normalized absorption spectrum.

At the beginning, 5 nm thickness was examined. Its absorbance was found lower than 1/2 that we do not consider it as a plasmonic layer candidate. It is only considered in Figure 5.10 to show the difference. In Figure 5.5, raw and normalized absorption data of 7.5, 10 and 12.5 nm silver nanoisland layers are given. The information on how these

measurements were implemented are given in Section 4.4.3. Figure 5.5a can be interpreted such that an increase in thickness causes absorption peaks to redshift while the absorption intensity increases. These peaks are the result of the coincidence of frequencies belonging to plasmons and incident field [100]. Due to larger nanoisland structures, 12.5 nm layer had a maximum at a longer wavelength and a broader spectrum (Figure 5.5b). Related peak wavelengths are shown in the legend of Figure 5.5b.

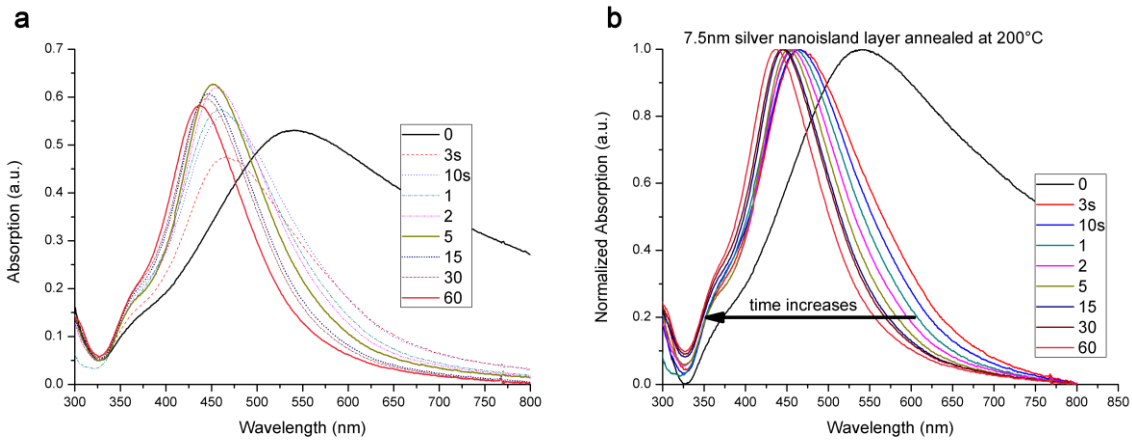

Figure 5.6: a) Absorption and b) normalized absorption of 7.5 nm silver nanoisland layer annealed for different durations.

Silver nanoisland layers with the thickness of 7.5 nm were annealed at 200°C inside the glovebox for 3s, 10s, 1min, 2 min, 5min, 15min, 30min and 60min durations (Figure 5.6). Even for 3s of annealing, the peak wavelength moved to blue side of the spectrum nearly 75nm. It was observed that the longer the annealing time, the shorter the absorption peak and linewidth (Figure 5.6b). However, it is not the case for the absorption intensity. The highest intensity for the layer of 7.5nm thickness was for 5 minutes of annealing. For longer durations, absorbance decreased. For peak vs. annealing time measurements which were obtained from these measurements (Table 5.1), a fitting was possible (Figure 5.7).

Annealing time	Peak wavelength
0	540 nm
3 seconds	465 nm
10 seconds	464 nm
1 minute	458.5 nm
2 minutes	454 nm
5 minutes	451 nm
15 minutes	446.5 nm
30 minutes	443.5 nm
60 minutes	437.5 nm

Table 5.1: Table for 7.5nm silver nanoisland layer annealed at 200°C, annealing time vs. peak absorption wavelength

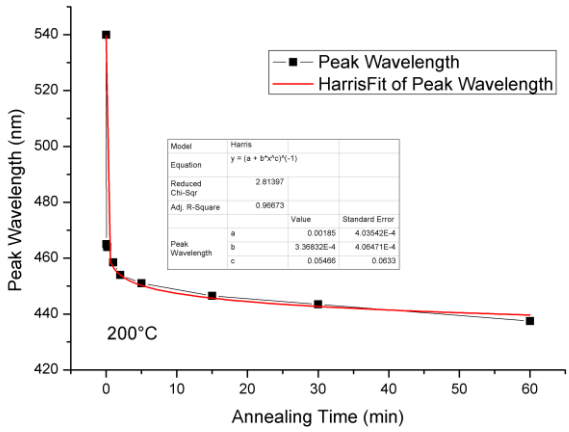

Figure 5.7: HarrisFit of data in Table 5.1.

Investigations were implemented on 10 nm and 12.5 nm layers, too. Likewise, blueshift with the increasing time was observed on these samples. Since 12.5 nm samples had the greater absorbance before annealing, a higher annealing temperature was experimented. 12.5 nm samples were annealed at 200°C and 300°C. In the same manner as 7.5 nm samples, 5 minutes of annealing had the greatest absorption at both temperatures (Figure 5.8). 200°C samples had the same peak (453 nm) for all annealing durations (Figure 5.8a). 300°C samples had shorter linewidth and blueshifted with annealing time (Figure 5.8b). Peak distribution vs. annealing time demonstrated similar trend as 7.5 nm (Figure 5.9).

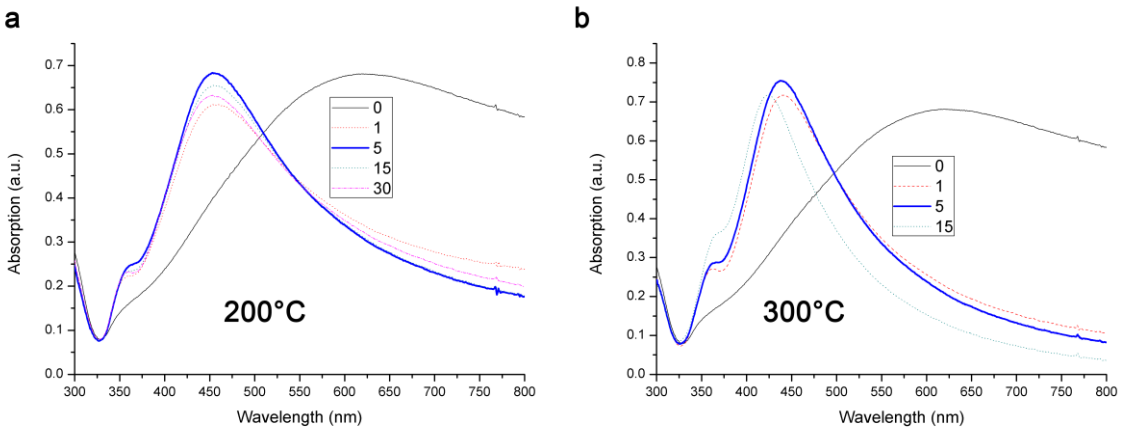

Figure 5.8: 12.5 nm silver nanoisland layers annealed at a)200°C and b)300°C. Legends show annealing time in min.

Annealing time	Peak wavelength
0	621 nm
1 minute	442 nm
5 minutes	438 nm
15 minutes	423 nm

Table 5.2: Table for 12.5nm silver nanoisland layer annealed at 300°C, annealing time vs. peak absorption wavelength

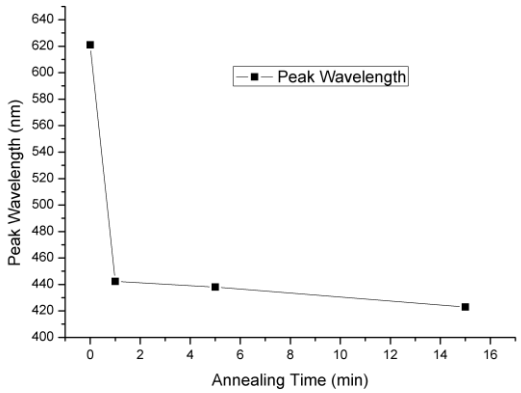

Figure 5.9: Graph of Table 5.2

Consequently, absorbance characteristics for 5 minutes of annealing are compared in Figure 5.10. 12.5 nm annealed at 300°C for 5 minutes exhibited greatest absorbance (Figure 5.10a) and the shortest linewidth (Figure 5.10b) among the samples. Therefore, this sample was picked for further use.

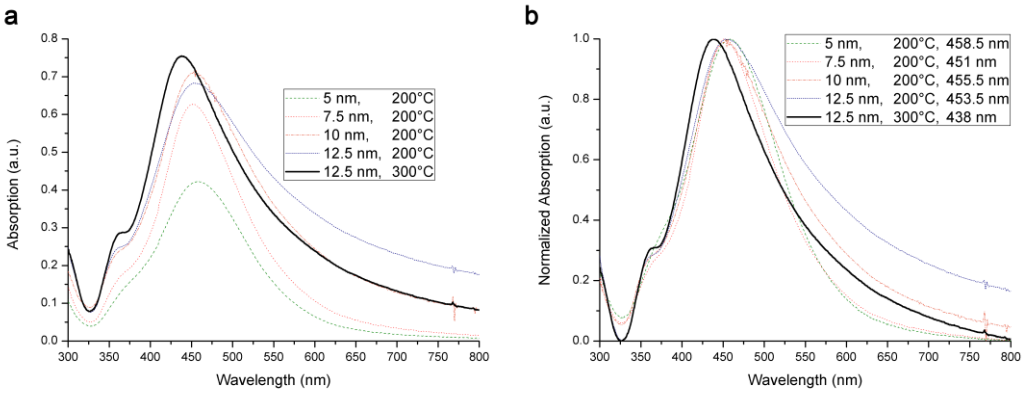

Figure 5.10: a) Absorption and b) normalized absorption of samples exposed to 5 minutes of annealing

A new sample was prepared using the same procedure. Raw and annealed surfaces were examined through AFM characterization (Figure 5.11). Measurements showed that annealing results in higher nanoislands with higher surface roughness. The cantilever used for AFM measurements has resonance frequency of 320 kHz and force constant of 42 N/m. In Figure 5.11a, silver nanoislands are homogeneous in shape and distribution. RMS roughness obtained from Figure 5.11a is 2.27 nm and maximum height is 17.7 nm. Figure 5.11b shows related 3D profile. On the other hand, annealing merges nanoislands and creates island areas with higher peaks while causing empty areas among nanoislands. Figure 5.11c belongs to 12.5 nm sample annealed at 300°C for 5 min gives RMS roughness of 11.48 nm with 81 nm maximum. Corresponding 3D profile is presented in Figure 5.11d. AFM measurements were consistent with the literature [100].

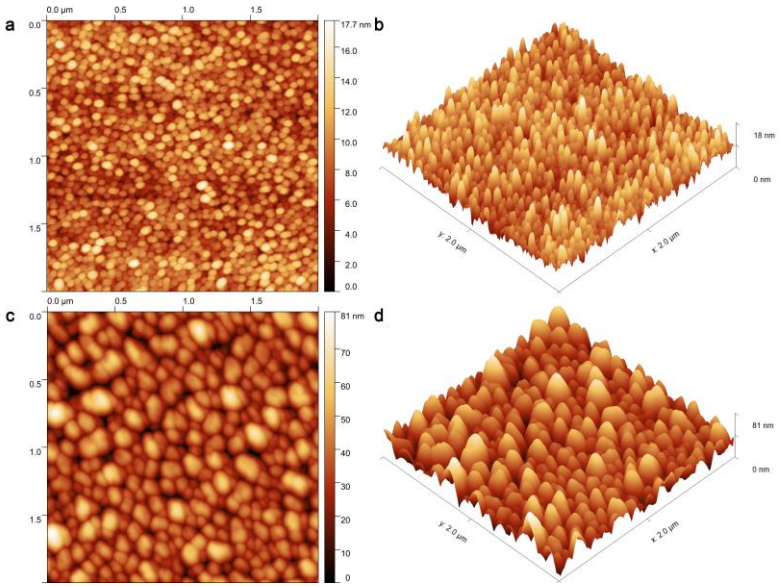

Figure 5.11: AFM measurement results of 12.5 nm silver nanoisland layer deposited with 0.1 Å/s a) and b) after deposition; c) and d) after annealing at 300°C for 5 min.

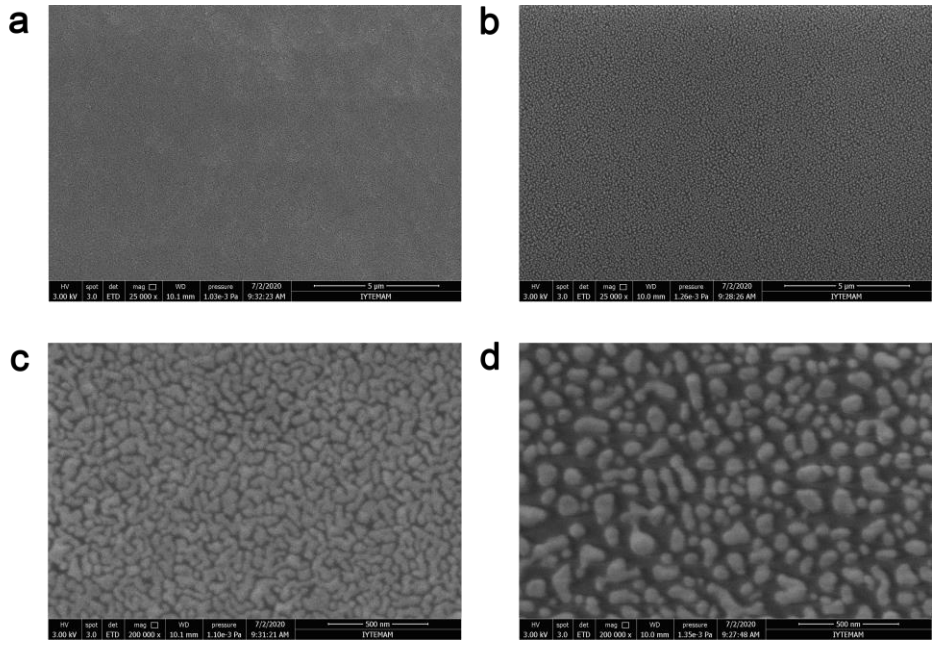

Figure 5.12: SEM images of 12.5 nm Ag layer deposited via thermal evaporation. 5 um scale images a) before and b) after annealing. 500 nm scale images c) before and d) after annealing.

SEM characterization proved the homogeneity and aggregation. Figure 5.12 shows SEM images of the samples given in Figure 5.13. As mentioned before, Figure 5.12a and 5.12b, which are images before and after annealing, respectively, have homogenous distribution. Under a smaller scaled observation, nanoislands are distinguishable (Figure 5.12c) and after annealing, island-to-island distance increases due to merging, which causes higher silver peaks (Figure 5.12d) as established by AFM measurements (Figure 5.11).

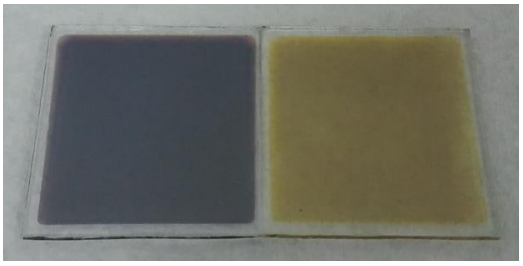

Figure 5.13: 12.5 nm silver a) before annealing, b) after annealing

Figure 5.13 shows images of 12.5 nm silver deposition before and after annealing. Consistent with the absorption characteristics, the raw layer has a purple color (under ambient light) resulting from higher absorbance in longer wavelengths, and annealed layer has a yellowish color arising from absorbance in bluish colors.

As the next, Al_2O_3 layer was deposited over 12.5 nm silver nanoisland layer which was annealed at 300°C for 5 minutes. For the purpose of observing the enhancement in

fluorescence step by step, deposition thicknesses were increased with 3nm steps up to 24 nm. Thus, 9 samples of 12.5 nm silver layer were prepared on quartz. Atomic Layer Deposition, which is explained in Section 4.2, was utilized to deposit alumina spacer layers. Peak absorption wavelength increased with the spacer thickness and the thickness caused widening in linewidth. The spacer layer on nanoislands acts as a shell on nanoparticle. Dielectric function of the shell material determines the shift. For this reason, another dielectric material such as SiO_2 would result in a different amount of redshift in every thickness. Absorption peaks for samples with different thickness values are given in Table 5.3. Corresponding normalized spectra are given in Figure 5.14.

Al_2O_3 spacer thickness (nm)	Absorption Peak (nm)
0	441
3	451
6	478
9	494
12	500
15	505
18	509
21	521
24	531

Table 5.3: Spacer thickness-peak wavelength table

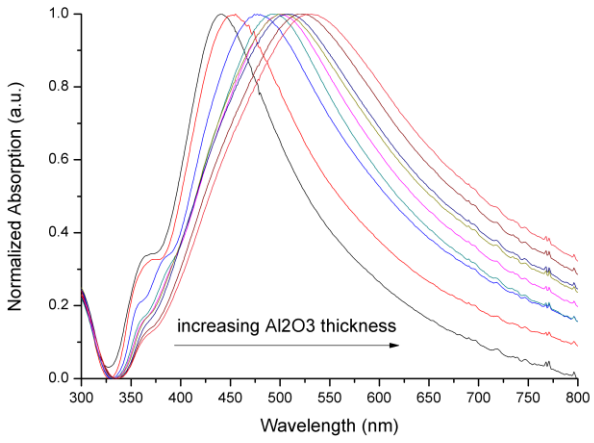

Figure 5.14: Normalized absorption for samples deposited with 3 nm steps of Al_2O_3

5.3. Combining Excitonic and Plasmonic Layers

PL characteristic of perovskite nanowires that was used in this study is given in Figure 5.15 with enhanced emissions. NWs in hexane were deposited on Al_2O_3/Ag/Quartz structure. Nanowires under the influence of silver nanoislands enhanced their PL emission as long as their separation is enough. The samples without sufficient distance got quenched PL.

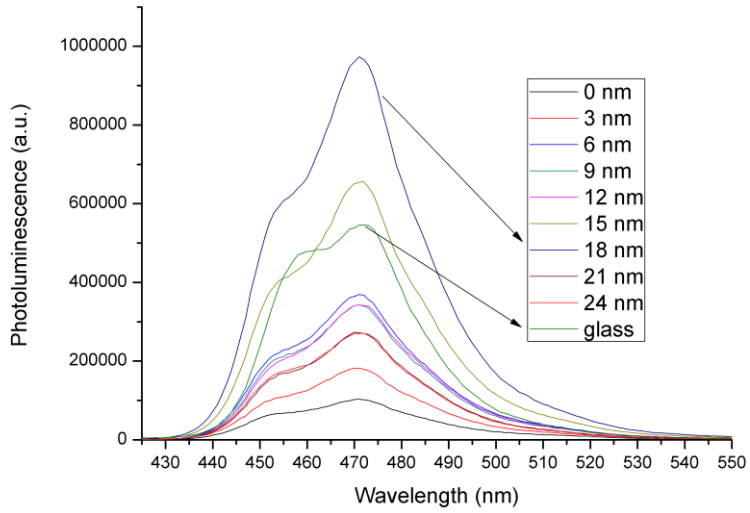

Figure 5.15: PL intensities with different spacer thicknesses. "glass" data belongs to perovskite deposited glass substrate.

The NW/Ag sample exhibited quenching of PL due to direct contact of emitter and metal. Emitter touching the metal causes excited electrons to decay over electronic states of metal. This happens due to nanowires' wavefunctions expanding beyond metal's borders. Placing a distance via a dielectric material (such as SiO_2, or Al_2O_3 as in this study) can prevent electron leakage. This spacer acts as a potential barrier for electrons, therefore the longer the distance, the lower the probability of tunneling. However, LSPs create a field enhancement very near to boundaries of metal nanoparticle. Therefore, there is a spacer thickness that satisfies the optimum for this trade-off. In accordance with this, for perovskite/Al_2O_3/Au samples the PL intensity increased towards and decreased beyond the optimum thickness (Figure 5.16). 18 nm sample showed maximum PL enhancement of 78.3%.

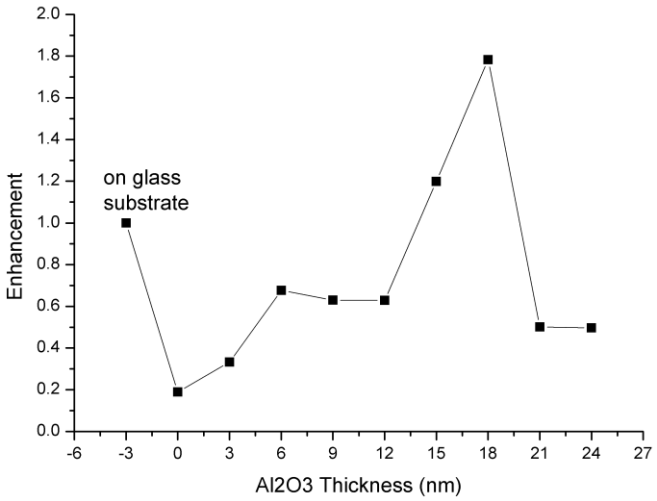

Figure 5.16: Field enhancement normalized to perovskite on glass data

TRPL measurements given in Figure 5.17 shows that radiative and nonradiative decay times changed. The downward change in lifetimes proves that the coupling is successful. For the perovskite/Ag sample the net difference of radiative and nonradiative decays resulted in quenching of PL intensity, therefore it has the fastest decay of all. Domination of radiative decays over nonradiative decays is the reason of enhancement in PL-enhanced samples. Intensity average lifetimes were calculated as 3.02, 0.84, 2.27, 2.06, 3.38, 4.1, 4.47, 4.55, 4.62 and 5.12 ns for glass and 0-24 nm data, respectively (Figure 5.17b).

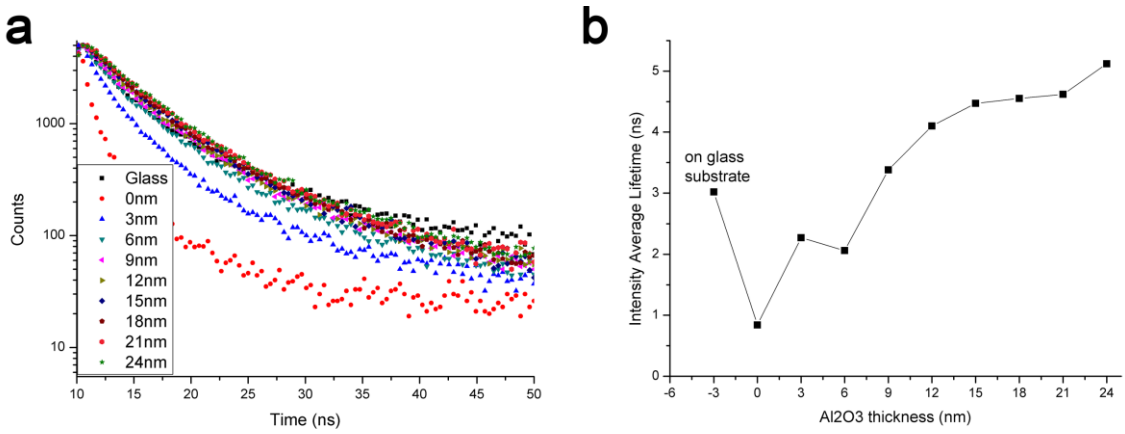

Figure 5.17: a)TRPL data, b) Intensity average lifetime vs. Al_2O_3 thickness

CONCLUSION

In this thesis we investigated consequences of LSP coupling with perovskite nanowires. Firstly, we examined perovskite structure, its properties, and their synthesis methods. Later, we gave information on surface plasmons and localized surface plasmons, and we discussed how they can be utilized and fabricated. After describing our experimental methods, we elucidated our aims and why we needed them in Experimental Results section. Consequently, we obtained 78.3 % of field enhancement when the Al_2O_3 layer thickness was 18 nm. 81.1% of PL quenching was observed for the condition where there was no distance between perovskite NWs and Ag nanoislands. PL-quenched samples had intensity average lifetime of 0.84 ns. As the thickness increases, we saw that lifetimes increase. We observed intensity average lifetimes greater than the on-glass sample and we attribute this to double gaussian emission in our nanocrystals, which is a result of emission from nanocrystals of two different sizes. If we had one gaussian emission, as a result of enhancement, we should have observed faster lifetimes and lifetimes would have increased up to the value of on-glass sample with increasing spacer thickness because increasing thickness lowers the effects of plasmons.

We hope that this study helps improvement of fluorescence enhancement studies and understanding the enhancement mechanism better.

REFERENCES

1. Katz, Eugene A. (2020) "Perovskite: Name Puzzle and German-Russian Odyssey of Discovery." Helvetica Chimica Acta.

2. Bahoosh, S. G., & Wesselinowa, J. M. (2012). The origin of magnetism in perovskite ferroelectric ABO3 nanoparticles (A= K, Li; B= Ta, Nb or A= Ba, Sr, Pb; B= Ti). Journal of Applied Physics, 112(5), 053907.

3. Ren, Lixia, Yutao Wang, Min Wang, Shuanhu Wang, Yang Zhao, Claudio Cazorla, Changle Chen, Tom Wu, and Kexin Jin. (2020) "Tuning Magnetism and Photocurrent in Mn-Doped Organic–Inorganic Perovskites." The Journal of Physical Chemistry Letters 11, no. 7: 2577-2584.

4. Zhu, H. X., X. H. Wang, and G. C. Zhuang. (2019) "Electronic structure, magnetism properties and optical absorption of organometal halide perovskite CH 3 NH 3 XI 3 (X= Fe, Mn)." Applied Physics A 125, no. 1: 45.

5. Ming, Wenmei, Hongliang Shi, and Mao-Hua Du. (2016) "Large dielectric constant, high acceptor density, and deep electron traps in perovskite solar cell material CsGeI 3." Journal of Materials Chemistry A 4, no. 36: 13852-13858.

6. Semwal, B. S., and N. S. Panwar. (1992) "Dielectric properties of perovskite crystals." Bulletin of Materials Science 15, no. 3: 237.

7. Cho, Seungho, Chao Yun, Yoon Seo Kim, Han Wang, Jie Jian, Wenrui Zhang, Jijie Huang, Xuejing Wang, Haiyan Wang, and Judith L. MacManus-Driscoll. (2018) "Strongly enhanced dielectric and energy storage properties in lead-free perovskite titanate thin films by alloying." Nano Energy 45: 398-406.

8. Wilson, Jacob N., Jarvist M. Frost, Suzanne K. Wallace, and Aron Walsh. (2019) "Dielectric and ferroic properties of metal halide perovskites." APL Materials 7, no. 1: 010901.

9. Nuraje, Nurxat, and Kai Su. (2013) "Perovskite ferroelectric nanomaterials." Nanoscale 5, no. 19: 8752-8780.

10. Gao, Wenxiu, Yi Zhu, Yaojin Wang, Guoliang Yuan, and Jun-Ming Liu. (2020) "A review of flexible perovskite oxide ferroelectric films and their application." Journal of Materiomics 6, no. 1: 1-16.

11. Wu, Liyan. (2019) "Investigation of Ferroelectric Perovskite Oxides for Photovoltaic Applications". *Dissertations available from ProQuest*. AAI22589459. https://repository.upenn.edu/dissertations/AAI22589459

12. Strelcov, Evgheni, Qingfeng Dong, Tao Li, Jungseok Chae, Yuchuan Shao, Yehao Deng, Alexei Gruverman, Jinsong Huang, and Andrea Centrone. (2017) "CH3NH3PbI3 perovskites: Ferroelasticity revealed." Science advances 3, no. 4: e1602165.

13. Liu, Yongtao, Liam Collins, Roger Proksch, Songkil Kim, Brianna R. Watson, Benjamin Doughty, Tessa R. Calhoun et al. (2018) "Chemical nature of ferroelastic twin domains in CH 3 NH 3 PbI 3 perovskite." Nature materials 17, no. 11: 1013-1019.

14. Eaton, Samuel W., Minliang Lai, Natalie A. Gibson, Andrew B. Wong, Letian Dou, Jie Ma, Lin-Wang Wang, Stephen R. Leone, and Peidong Yang. (2016) "Lasing in robust cesium lead halide perovskite nanowires." Proceedings of the National Academy of Sciences 113, no. 8: 1993-1998.

15. Li, Ying, Shuting Guan, Yi Liu, Gongjie Xu, and Bin Cai. (2018) "Lasing properties of cesium lead halide perovskite nanowires fabricated by one-drop self-assembly and ion-exchange methods." Optics Express 26, no. 26: 33856-33864.

16. Zhang, Qing, Rui Su, Wenna Du, Xinfeng Liu, Liyun Zhao, Son Tung Ha, and Qihua Xiong. (2017) "Advances in small perovskite-based lasers." Small Methods 1, no. 9: 1700163.

17. Shi, Zhi-Feng, Xu-Guang Sun, Di Wu, Ting-Ting Xu, Yong-Tao Tian, Yuan-Tao Zhang, Xin-Jian Li, and Guo-Tong Du. (2016) "Near-infrared random lasing realized in a perovskite CH 3 NH 3 PbI 3 thin film." Journal of Materials Chemistry C 4, no. 36: 8373-8379.

18. Ohl, R. S. (1946). U.S. Patent No. 2,402,662. Washington, DC: U.S. Patent and Trademark Office.

19. Yoshikawa, Kunta, Hayato Kawasaki, Wataru Yoshida, Toru Irie, Katsunori Konishi, Kunihiro Nakano, Toshihiko Uto et al. (2017) "Silicon heterojunction solar cell with interdigitated back contacts for a photoconversion efficiency over 26%." Nature energy 2, no. 5: 17032.

20. Levi, Dean H., Martin A. Green, Yoshihiro Hishikawa, Ewan D. Dunlop, Jochen Hohl-Ebinger, and Anita WY Ho-Baillie. (2017) "Solar cell efficiency tables (version 51)." Progress in Photovoltaics 26, no. NREL/JA-5J00-70757.

21. Andreani, Lucio Claudio, Angelo Bozzola, Piotr Kowalczewski, Marco Liscidini, and Lisa Redorici. (2019) "Silicon solar cells: toward the efficiency limits." Advances in Physics: X 4, no. 1: 1548305.

22. Kojima, Akihiro, Kenjiro Teshima, Yasuo Shirai, and Tsutomu Miyasaka. (2009) "Organometal halide perovskites as visible-light sensitizers for photovoltaic cells." Journal of the American Chemical Society 131, no. 17: 6050-6051.

23. Li, Yan, Robert LZ Hoye, Huan-Huan Gao, Lihe Yan, Xiaoyong Zhang, Yong Zhou, Judith L. MacManus-Driscoll, and Jiantuo Gan. (2020) "Over 20% Efficiency in Methylammonium Lead Iodide Perovskite Solar Cells with Enhanced Stability via “in Situ Solidification” of the TiO2 Compact Layer." ACS Applied Materials & Interfaces 12, no. 6: 7135-7143.

24. Saliba, Michael, Juan-Pablo Correa-Baena, Christian M. Wolff, Martin Stolterfoht, Nga Phung, Steve Albrecht, Dieter Neher, and Antonio Abate. (2018) "How to Make over 20% Efficient Perovskite Solar Cells in Regular (n–i–p) and Inverted (p–i–n) Architectures." Chemistry of Materials 30, no. 13: 4193-4201.

25. Chen, Zhaolai, Bekir Turedi, Abdullah Y. Alsalloum, Chen Yang, Xiaopeng Zheng, Issam Gereige, Ahmed AlSaggaf, Omar F. Mohammed, and Osman M. Bakr. (2019) "Single-crystal MAPbI3 perovskite solar cells exceeding 21% power conversion efficiency." ACS Energy Letters 4, no. 6: 1258-1259.

26. Hong, X., T. Ishihara, and A. V. Nurmikko. (1992) "Photoconductivity and electroluminescence in lead iodide based natural quantum well structures." Solid state communications 84, no. 6: 657-661.

27. Nedelcu, Georgian, Loredana Protesescu, Sergii Yakunin, Maryna I. Bodnarchuk, Matthias J. Grotevent, and Maksym V. Kovalenko. (2015) "Fast anion-exchange in highly luminescent nanocrystals of cesium lead halide perovskites (CsPbX3, X= Cl, Br, I)." Nano letters 15, no. 8: 5635-5640.

28. Creutz, Sidney E., Evan N. Crites, Michael C. De Siena, and Daniel R. Gamelin. (2018) "Anion exchange in cesium lead halide perovskite nanocrystals and thin films using trimethylsilyl halide reagents." Chemistry of Materials 30, no. 15: 4887-4891.

29. Zhang, Ye, Dylan Lu, Mengyu Gao, Minliang Lai, Jia Lin, Teng Lei, Zhenni Lin, Li Na Quan, and Peidong Yang. (2019) "Quantitative imaging of anion exchange kinetics in halide perovskites." Proceedings of the National Academy of Sciences 116, no. 26: 12648-12653.

30. Pisanu, Ambra, Paolo Quadrelli, and Lorenzo Malavasi. (2019) "Facile anion-exchange reaction in mixed-cation lead bromide perovskite nanocrystals." RSC advances 9, no. 23: 13263-13268.

31. Akkerman, Quinten A., Valerio D’Innocenzo, Sara Accornero, Alice Scarpellini, Annamaria Petrozza, Mirko Prato, and Liberato Manna. (2015) "Tuning the optical properties of cesium lead halide perovskite nanocrystals by anion exchange reactions." Journal of the American Chemical Society 137, no. 32: 10276-10281.

32. Bekenstein, Yehonadav, Brent A. Koscher, Samuel W. Eaton, Peidong Yang, and A. Paul Alivisatos. (2015) "Highly luminescent colloidal nanoplates of perovskite cesium lead halide and their oriented assemblies." Journal of the American Chemical Society 137, no. 51: 16008-16011.

33. Wei, Song, Yanchun Yang, Xiaojiao Kang, Lan Wang, Lijian Huang, and Daocheng Pan. (2016) "Room-temperature and gram-scale synthesis of CsPbX 3 (X= Cl, Br, I) perovskite nanocrystals with 50–85% photoluminescence quantum yields." Chemical Communications 52, no. 45: 7265-7268.

34. Li, Yang, Liubing Dong, Nan Chen, Ziquan Guo, Ying Lv, Jianghui Zheng, and Chao Chen. (2019) "Room-temperature synthesis of two-dimensional hexagonal boron nitride nanosheet-stabilized CsPbBr3 perovskite quantum dots." ACS Applied Materials & Interfaces 11, no. 8: 8242-8249.

35. Microscopy Australia, accessed 10.06.2020, <https://www.myscope.training>

36. Amgar, Daniel, Avigail Stern, Dvir Rotem, Danny Porath, and Lioz Etgar. (2017) "Tunable length and optical properties of CsPbX3 (X= Cl, Br, I) nanowires with a few unit cells." Nano letters 17, no. 2: 1007-1013.

37. Huang, He, Lakshminarayana Polavarapu, Jasmina A. Sichert, Andrei S. Susha, Alexander S. Urban, and Andrey L. Rogach. (2016) "Colloidal lead halide perovskite nanocrystals: synthesis, optical properties and applications." NPG Asia Materials 8, no. 11: e328-e328.

38. Manser, Joseph S., Jeffrey A. Christians, and Prashant V. Kamat. (2016) "Intriguing optoelectronic properties of metal halide perovskites." Chemical reviews 116, no. 21: 12956-13008.

39. Philippe, Bertrand, T. Jesper Jacobsson, Juan-Pablo Correa-Baena, Naresh K. Jena, Amitava Banerjee, Sudip Chakraborty, Ute B. Cappel et al. (2017) "Valence level character in a mixed perovskite material and determination of the valence band maximum from photoelectron spectroscopy: variation with photon energy." The Journal of Physical Chemistry C 121, no. 48: 26655-26666.

40. Meloni, Simone, Giulia Palermo, Negar Ashari-Astani, Michael Grätzel, and Ursula Rothlisberger. (2016) "Valence and conduction band tuning in halide perovskites for solar cell applications." Journal of Materials Chemistry A 4, no. 41: 15997-16002.

41. Xing, Jun, Fei Yan, Yawen Zhao, Shi Chen, Huakang Yu, Qing Zhang, Rongguang Zeng et al. (2016) "High-efficiency light-emitting diodes of organometal halide perovskite amorphous nanoparticles." ACS nano 10, no. 7: 6623-6630.

42. Du, Xiafang, Guan Wu, Jian Cheng, Hui Dang, Kangzhe Ma, Ya-Wen Zhang, Peng-Feng Tan, and Su Chen. (2017) "High-quality CsPbBr 3 perovskite nanocrystals for quantum dot light-emitting diodes." RSC advances 7, no. 17: 10391-10396.

43. Sadhanala, Aditya, Shahab Ahmad, Baodan Zhao, Nadja Giesbrecht, Phoebe M. Pearce, Felix Deschler, Robert LZ Hoye et al. (2015) "Blue-green color tunable solution processable organolead chloride–bromide mixed halide perovskites for optoelectronic applications." Nano letters 15, no. 9: 6095-6101.

44. Protesescu, Loredana, Sergii Yakunin, Maryna I. Bodnarchuk, Franziska Krieg, Riccarda Caputo, Christopher H. Hendon, Ruo Xi Yang, Aron Walsh, and Maksym V. Kovalenko. (2015) "Nanocrystals of cesium lead halide perovskites (CsPbX3, X= Cl, Br, and I): novel optoelectronic materials showing bright emission with wide color gamut." Nano letters 15, no. 6: 3692-3696.

45. Choi, Yung Ji, Lamjed Debbichi, Do-Kyoung Lee, Nam-Gyu Park, Hyungjun Kim, and Dongho Kim. (2019) "Light Emission Enhancement by Tuning the Structural Phase of APbBr3 (A= CH3NH3, Cs) Perovskites." The journal of physical chemistry letters 10, no. 9: 2135-2142.

46. Kang, Jun, and Lin-Wang Wang. (2017) "High defect tolerance in lead halide perovskite CsPbBr3." The journal of physical chemistry letters 8, no. 2: 489-493.

47. Huang, He, Maryna I. Bodnarchuk, Stephen V. Kershaw, Maksym V. Kovalenko, and Andrey L. Rogach. (2017) "Lead halide perovskite nanocrystals in the research spotlight: Stability and defect tolerance." ACS energy letters 2, no. 9: 2071-2083.

48. Pandey, Mohnish, Karsten W. Jacobsen, and Kristian S. Thygesen. (2016) "Band gap tuning and defect tolerance of atomically thin two-dimensional organic–inorganic halide perovskites." The journal of physical chemistry letters 7, no. 21: 4346-4352.

49. Yan, Fei, Jun Xing, Guichuan Xing, Lina Quan, Swee Tiam Tan, Jiaxin Zhao, Rui Su et al. (2018) "Highly efficient visible colloidal lead-halide perovskite nanocrystal light-emitting diodes." Nano letters 18, no. 5: 3157-3164.

50. Lin, Kebin, Jun Xing, Li Na Quan, F. Pelayo García de Arquer, Xiwen Gong, Jianxun Lu, Liqiang Xie et al. (2018) "Perovskite light-emitting diodes with external quantum efficiency exceeding 20 per cent." Nature 562, no. 7726: 245-248.

51. Song, Jizhong, Tao Fang, Jianhai Li, Leimeng Xu, Fengjuan Zhang, Boning Han, Qingsong Shan, and Haibo Zeng. (2018) "Organic–inorganic hybrid passivation enables perovskite QLEDs with an EQE of 16.48%." Advanced Materials 30, no. 50: 1805409.

52. Yang, Xiaolei, Xingwang Zhang, Jinxiang Deng, Zema Chu, Qi Jiang, Junhua Meng, Pengyang Wang, Liuqi Zhang, Zhigang Yin, and Jingbi You. (2018) "Efficient green light-emitting diodes based on quasi-two-dimensional composition and phase engineered perovskite with surface passivation." Nature communications 9, no. 1: 1-8.

53. Wang, Yue, Xiaoming Li, Jizhong Song, Lian Xiao, Haibo Zeng, and Handong Sun. (2015) "All-inorganic colloidal perovskite quantum dots: a new class of lasing materials with favorable characteristics." Advanced materials 27, no. 44: 7101-7108.

54. Yakunin, Sergii, Loredana Protesescu, Franziska Krieg, Maryna I. Bodnarchuk, Georgian Nedelcu, Markus Humer, Gabriele De Luca, Manfred Fiebig, Wolfgang Heiss, and Maksym V. Kovalenko. (2015) "Low-threshold amplified spontaneous

emission and lasing from colloidal nanocrystals of caesium lead halide perovskites." Nature communications 6, no. 1: 1-9.

55. Tang, Xiaosheng, Yao Bian, Zhengzheng Liu, Juan Du, Meng Li, Zhiping Hu, Jie Yang, Weiwei Chen, and Lidong Sun. (2019) "Room-temperature up-conversion random lasing from CsPbBr 3 quantum dots with TiO 2 nanotubes." Optics Letters 44, no. 19: 4706-4709.

56. Su, Rui, Carole Diederichs, Jun Wang, Timothy CH Liew, Jiaxin Zhao, Sheng Liu, Weigao Xu, Zhanghai Chen, and Qihua Xiong. (2017) "Room-temperature polariton lasing in all-inorganic perovskite nanoplatelets." Nano letters 17, no. 6: 3982-3988.

57. Stranks, Samuel D. (2017) "Nonradiative losses in metal halide perovskites." ACS Energy Letters 2, no. 7: 1515-1525.

58. Deschler, Felix, Michael Price, Sandeep Pathak, Lina E. Klintberg, David-Dominik Jarausch, Ruben Higler, Sven Hüttner et al. (2014) "High photoluminescence efficiency and optically pumped lasing in solution-processed mixed halide perovskite semiconductors." The journal of physical chemistry letters 5, no. 8: 1421-1426.

59. Abdi-Jalebi, Mojtaba, Zahra Andaji-Garmaroudi, Stefania Cacovich, Camille Stavrakas, Bertrand Philippe, Johannes M. Richter, Mejd Alsari et al. (2018) "Maximizing and stabilizing luminescence from halide perovskites with potassium passivation." Nature 555, no. 7697: 497-501.

60. Braly, Ian L., Dane W. deQuilettes, Luis M. Pazos-Outón, Sven Burke, Mark E. Ziffer, David S. Ginger, and Hugh W. Hillhouse. (2018) "Hybrid perovskite films approaching the radiative limit with over 90% photoluminescence quantum efficiency." Nature Photonics 12, no. 6: 355-361.

61. Brenes, Roberto, Dengyang Guo, Anna Osherov, Nakita K. Noel, Christopher Eames, Eline M. Hutter, Sandeep K. Pathak et al. (2017) "Metal halide perovskite polycrystalline films exhibiting properties of single crystals." Joule 1, no. 1: 155-167.

62. Kim, Young-Hoon, Himchan Cho, and Tae-Woo Lee. (2016) "Metal halide perovskite light emitters." Proceedings of the National Academy of Sciences 113, no. 42: 11694-11702.

63. Lozano, Gabriel. (2018) "The role of metal halide perovskites in next-generation lighting devices." The journal of physical chemistry letters 9, no. 14: 3987-3997.

64. Kovalenko, Maksym V., Loredana Protesescu, and Maryna I. Bodnarchuk. (2017) "Properties and potential optoelectronic applications of lead halide perovskite nanocrystals." Science 358, no. 6364: 745-750.

65. Wei, Song, Yanchun Yang, Xiaojiao Kang, Lan Wang, Lijian Huang, and Daocheng Pan. (2016) "Room-temperature and gram-scale synthesis of CsPbX 3 (X= Cl, Br, I)

perovskite nanocrystals with 50–85% photoluminescence quantum yields." Chemical Communications 52, no. 45: 7265-7268.

66. Li, Xiaoming, Ye Wu, Shengli Zhang, Bo Cai, Yu Gu, Jizhong Song, and Haibo Zeng. (2016) "CsPbX3 quantum dots for lighting and displays: room-temperature synthesis, photoluminescence superiorities, underlying origins and white light-emitting diodes." Advanced Functional Materials 26, no. 15: 2435-2445.

67. Kumar, Sudhir, Jakub Jagielski, Tommaso Marcato, Simon F. Solari, and Chih-Jen Shih. (2019) "Understanding the Ligand Effects on Photophysical, Optical, and Electroluminescent Characteristics of Hybrid Lead Halide Perovskite Nanocrystal Solids." The journal of physical chemistry letters 10, no. 24: 7560-7567.

68. Bekenstein, Yehonadav, Brent A. Koscher, Samuel W. Eaton, Peidong Yang, and A. Paul Alivisatos. (2015) "Highly luminescent colloidal nanoplates of perovskite cesium lead halide and their oriented assemblies." Journal of the American Chemical Society 137, no. 51: 16008-16011.

69. Zhang, Dandan, Samuel W. Eaton, Yi Yu, Letian Dou, and Peidong Yang. (2015) "Solution-phase synthesis of cesium lead halide perovskite nanowires." Journal of the American Chemical Society 137, no. 29: 9230-9233.

70. Shamsi, Javad, Zhiya Dang, Paolo Bianchini, Claudio Canale, Francesco Di Stasio, Rosaria Brescia, Mirko Prato, and Liberato Manna. (2016) "Colloidal synthesis of quantum confined single crystal CsPbBr3 nanosheets with lateral size control up to the micrometer range." Journal of the American Chemical Society 138, no. 23: 7240-7243.

71. Jain, Anubhav, Ivano E. Castelli, Geoffroy Hautier, David H. Bailey, and Karsten W. Jacobsen. (2013) "Performance of genetic algorithms in search for water splitting perovskites." Journal of Materials Science 48, no. 19: 6519-6534.

72. Sambles, J. R., G. W. Bradbery, and Fuzi Yang. (1991) "Optical excitation of surface plasmons: an introduction." Contemporary physics 32, no. 3: 173-183.

73. Raether, H. (1977) "Surface plasma oscillations and their applications.".

74. Purcell, Edward M., Henry Cutler Torrey, and Robert V. Pound. (1946) "Resonance absorption by nuclear magnetic moments in a solid." Physical review 69, no. 1-2: 37.

75. Barnes, William L., Alain Dereux, and Thomas W. Ebbesen. (2003) "Surface plasmon subwavelength optics." nature 424, no. 6950: 824-830.

76. Otto, A. (1968) "Eine neue methode der anregung nichtstrahlender oberflächenplasmaschwingungen." physica status solidi (b) 26, no. 2: K99-K101.

77. Kretschmann, Erwin, and Heinz Raether. (1968) "Radiative decay of non-radiative surface plasmons excited by light." Z. Naturforsch. a 23, no. 12: 2135-2136.

78. Moharam, M. G., and Thomas K. Gaylord. (1986) "Rigorous coupled-wave analysis of metallic surface-relief gratings." JOSA a 3, no. 11: 1780-1787.

79. Mie, Gustav. (1908) "Beiträge zur Optik trüber Medien, speziell kolloidaler Metallösungen." Annalen der physik 330, no. 3: 377-445.

80. Sönnichsen, Carsten. (2001) "Plasmons in metal nanostructures." PhD diss., lmu.

81. Soğancı, İbrahim Murat. (2007) "Localized plasmon-coupled semiconductor nanocrystal emitters for innovative device applications." PhD diss., Bilkent University.

82. Link, Stephan, and Mostafa A. El-Sayed. (1999) "Size and temperature dependence of the plasmon absorption of colloidal gold nanoparticles." The Journal of Physical Chemistry B 103, no. 21: 4212-4217.

83. Tam, Felicia, Glenn P. Goodrich, Bruce R. Johnson, and Naomi J. Halas. (2007) "Plasmonic enhancement of molecular fluorescence." Nano letters 7, no. 2: 496-501.

84. Gao, Mengyao, Xuanli Zheng, Imran Khan, Haoyuan Cai, Jinshen Lan, Jing Liu, Jiayuan Wang et al. (2019) "Resonant light absorption and plasmon tunability of lateral triangular Au nanoprisms array." Physics Letters A 383, no. 31: 125881.

85. Ashok, Anchu, Arya Arackal, and George Jacob. (2015) "Study of surface plasmon excitation on different structures of gold and silver." Nanosci. Nanotechnol 5, no. 4: 71-81.

86. Yu, Huakang, Yusi Peng, Yong Yang, and Zhi-Yuan Li. (2019) "Plasmon-enhanced light–matter interactions and applications." npj Computational Materials 5, no. 1: 1-14.

87. Anger, Pascal, Palash Bharadwaj, and Lukas Novotny. (2006) "Enhancement and quenching of single-molecule fluorescence." Physical review letters 96, no. 11: 113002.

88. Mattox, Donald M. (2010) Handbook of physical vapor deposition (PVD) processing. William Andrew.

89. Harsha, KSKS Sree. (2005) Principles of vapor deposition of thin films. Elsevier.

90. Albaigés, Joan, Josep M. Bayona, and Jagoš R. Radović. (2016) "Photochemical effects on oil spill fingerprinting." In Standard Handbook Oil Spill Environmental Forensics, pp. 917-959. Academic Press.

91. Novotny, Lukas, and Bert Hecht. (2012) Principles of nano-optics. Cambridge university press.

92. Gu, Xuefeng, Teng Qiu, Wenjun Zhang, and Paul K. Chu. (2011) "Light-emitting diodes enhanced by localized surface plasmon resonance." Nanoscale research letters 6, no. 1: 199.

93. Yeh, Dong-Ming, Cheng-Yen Chen, Yen-Cheng Lu, Chi-Feng Huang, and C. C. Yang. (2007) "Formation of various metal nanostructures with thermal annealing to control the effective coupling energy between a surface plasmon and an InGaN/GaN quantum well." Nanotechnology 18, no. 26: 265402.

94. Eppler, Aaron S., Günther Rupprechter, László Guczi, and Gabor A. Somorjai. (1997) "Model catalysts fabricated using electron beam lithography and pulsed laser deposition." The Journal of Physical Chemistry B 101, no. 48: 9973-9977.

95. Pompa, P. P., L. Martiradonna, A. Della Torre, F. Della Sala, L. Manna, M. De Vittorio, F. Calabi, R. Cingolani, and R. Rinaldi. (2006) "Metal-enhanced fluorescence of colloidal nanocrystals with nanoscale control." Nature nanotechnology 1, no. 2: 126-130.

96. Huang, Wenyu, Wei Qian, and Mostafa A. El-Sayed. (2005) "Optically detected coherent picosecond lattice oscillations in two dimensional arrays of gold nanocrystals of different sizes and shapes induced by femtosecond laser pulses." In Plasmonics: Metallic Nanostructures and Their Optical Properties III, vol. 5927, p. 592701. International Society for Optics and Photonics.

97. Carminati, Rémi, J-J. Greffet, Carsten Henkel, and Jean-Marie Vigoureux. (2006) "Radiative and non-radiative decay of a single molecule close to a metallic nanoparticle." Optics Communications 261, no. 2: 368-375.

98. Owen, Valerie. (1997) "Real-time optical immunosensors—A commercial reality." Biosensors and Bioelectronics 12, no. 1: i-ii.

99. Shpacovitch, Victoria. (2012) "Application of surface plasmon resonance (SPR) for the detection of single viruses and single biological nano-objects." J. Bacteriol. Parasitol 3, no. 7: e110.

100. Sockalingum, G. D., A. Beljebbar, H. Morjani, J. F. Angiboust, and M. Manfait. (1998) "Characterization of island films as surface-enhanced Raman spectroscopy substrates for detecting low antitumor drug concentrations at single cell level." Biospectroscopy 4, no. S5: S71-S78.